Supporting Information

for

Pulsed Laser-patterned high-entropy single-atomic sites and alloy coordinated graphene oxide for pH-universal water electrolysis

Yeryeong Lee [a,†], Jayaraman Theerthagiri [a,†], Wanwisa Limphirat [b,†], Ganga Periyasamy [c], Gyoung Hwa Jeong [d], Soorathep Kheawhom [e,*], Yongbing Tang [f], Myong Yong Choi [a,g,*]

[a] Department of Chemistry (BK21 FOUR), Research Institute of Natural Sciences, Gyeongsang National University, Jinju 52828, Republic of Korea

[b] Beamline Division, Synchrotron Light Research Institute (SLRI), Nakhon Ratchasima, 30000 Thailand

[c] Department of Chemistry, Bangalore University, Jnana Bharathi Campus, Bangalore 560056, India

[d] Research Institute for Green Energy Convergence Technology, Gyeongsang National University, Jinju, 52828, Republic of Korea

[e] Department of Chemical Engineering, Faculty of Engineering, Chulalongkorn University, Bangkok, 10330 Thailand

[f] Advanced Energy Storage Technology Research Center, Shenzhen Institutes of Advanced Technology, Chinese Academy of Sciences, Shenzhen 518055, China

[g] Core-Facility Center for Photochemistry & Nanomaterials, Gyeongsang National University, Jinju 52828, Republic of Korea

*Correspondence: soorathep.k@chula.ac.th (S. Kheawhom); mychoi@gnu.ac.kr (M.Y. Choi)

† These authors contributed equally to this work

Table of Contents

Figures:

Figure S11. (a) HER polarization graphs of HESAC–HEA/GO–Fe^{2+} and commercial Pt/C in 0.5 M H_2SO_4 and 1.0 M KOH solutions at 5 mV/s, and (b) η at 10 mA/cm^2.

Figure S12. Comparison of HER activity with overpotential and Tafel slope of HESAC–HEA/GO–Fe^{2+} and HESAC–HEA/GO–Fe^{3+} electrocatalysts in different electrolyte media.

Figure S13. The CV profiles for the synthesized HESAC-HEA/GO-Fe^{2+} and HESAC-HEA/GO-Fe^{3+} catalysts obtained in the potential window of -0.1 to 1.2 V vs. RHE at 50 mV/s in different electrolytes.

Figure S14. The evaluated TOF value at wide HER potential for the synthesized HESAC-HEA/GO-Fe^{2+} and HESAC-HEA/GO-Fe^{3+} in different electrolytes.

Figure S15. The evaluated mass activity at wide HER potential for the synthesized HESAC-HEA/GO-Fe^{2+} and HESAC-HEA/GO-Fe^{3+} in different electrolytes.

Figure S16. The fitted Nyquist impedance plot of HESAC-HEA/GO-Fe^{2+} and HESAC-HEA/GO-Fe^{3+} in different electrolytes measured at −0.136 V vs. RHE (Inset show fitted Randles equivalent circuit).

Figure S17. The extracted charge-transfer resistance (R_{ct}) value from the Nyquist impedance plot of HESAC-HEA/GO-Fe^{2+} and HESAC-HEA/GO-Fe^{3+} in different electrolytes measured at −0.136 V vs. RHE.

Figure S18. CV profiles of HESAC-HEA/GO-Fe^{2+} and HESAC-HEA/GO-Fe^{3+} catalysts measured in the non-Faradic portion in 0.5 M H_2SO_4, 1.0 M KOH, and 0.1 M $KClO_4$ electrolytes at different scan rate from 20-100 mV/s.

Figure S19. (a) OER polarization graphs of HESAC–HEA/GO–Fe^{2+} and commercial RuO_2 in 1.0 M KOH solution at 5 mV/s, and (b) η at 10 mA/cm^2.

Figure S20. Comparison of OER activity with overpotential and Tafel slope of HESAC–HEA/GO–Fe^{2+} and HESAC–HEA/GO–Fe^{3+} electrocatalysts in different electrolyte media.

Figure S21. The evaluated TOF value at wide OER potential for the synthesized HESAC-HEA/GO-Fe^{2+} and HESAC-HEA/GO-Fe^{3+} in different electrolytes.

Figure S22. The fitted Nyquist impedance plot of HESAC-HEA/GO-Fe^{2+} and HESAC-HEA/GO-Fe^{3+} in different electrolytes measured at **−0.136 V vs. RHE** (Inset show fitted Randles equivalent circuit).

Figure S23. The extracted charge-transfer resistance (R_{ct}) value from the Nyquist impedance plot of HESAC-HEA/GO-Fe^{2+} and HESAC-HEA/GO-Fe^{3+} in different electrolytes measured at −0.136 V vs. RHE.

Figure S24. The evaluated mass activity at wide OER potential for the synthesized HESAC-HEA/GO-Fe^{2+} and HESAC-HEA/GO-Fe^{3+} in different electrolytes.

Figure S25. The cell voltage required to deliver various current density for the fabricated HESAC–HEA/GO–Fe^{2+}‖HESAC–HEA/GO–Fe^{2+} electrolyzer in 1.0 M KOH and 0.5 M H_2SO_4 electrolytes.

Figure S26. Polarization curves of the fabricated IrO_2 ‖ Pt/C, IrO_2 ‖ HESAC-HEA/GO-Fe^{2+}, and IrO_2 ‖ HESAC-HEA/GO-Fe^{3+} in 0.5 M H_2SO_4 and 1.0 M KOH electrolytes.

Figure S27. Pictorial representation of the fabricated two-electrode membrane-less electrolyzer.

Figure S28. (a) FESEM and (b) EDS mapping of analysis of HESAC–HEA/GO–Fe^{2+} anode electrode fabricated on CC substrate after long-term OWS test.

Figure S29. XPS spectra of the HESAC–HEA/GO–Fe^{2+} anode electrode fabricated on CC substrate after long-term OWS test: (a) full-survey, (b) C 1*s*, (c) O 1*s*, (d) Co 2*p*, (e) Fe 2*p*, (f) Ni 2*p*, (g) Pt 4*f*, (h) Pd 3*d*, and (i) Ru 3*p*.

Figure S30. Various configuration of CoFeNiPtPdRu HEA optimized in this work. From this lowest energy k1 and k1a configuration used for catalytic adsorption studies.

Figure S31. (a) Reaction energy profile for water dissociation, (b) H-adsorption on various catalytic sites of CoFeNiPtPdRu, k1a HEA surface, and (c) the k1a atomic configuration of HEA.

Figure S32. Optimized atomic configuration of all catalytic sites for k1 model.

Figure S33. Optimized atomic configuration of all catalytic sites for k1a model.

Figure SI.1. Pre-electrochemical activation of the fabricated HESAC–HEA/GO–Fe^{2+} electrode on carbon cloth substrate through 200 continuous CV sweeps for HER and OER at a 50 mV s^{-1} in 1.0-M KOH

Figure SI.2. Pre-electrochemical activation of the fabricated HESAC–HEA/GO–Fe^{2+} electrode on carbon cloth substrate through 200 continuous CV sweeps for HER and OER at a 50 mV s^{-1} in 0.5-M H_2SO_4.

Tables:

Table S1. ICP-OES elemental ratio for HESAC-HEA/GO-Fe^{2+}, and HESAC-HEA/GO-Fe^{3+}.

Table S2. HER of the fabricated HESAC–HEA/GO–Fe^{2+} sample compared with the earlier reported HEA-based electrocatalysts.

Table S3. OER of the fabricated HESAC–HEA/GO–Fe^{2+} sample compared with the earlier reported HEA-based electrocatalysts.

S1. Materials

Iron(II) chloride tetrahydrate ($FeCl_2 \cdot 6H_2O$, ≥99%), potassium tetrachloroplatinate(II) (K_2PtCl_4, ≥98%), potassium palladinum(II) chloride (K_2PdCl_4, ≥98%), ruthenium(III) chloride hydrate ($RuCl_3 \cdot xH_2O$, ≥98%), and Nafion (5 wt.%) solution were purchased from Sigma Aldrich, USA. Nickel(II) chloride hexahydrate ($NiCl_2 \cdot 6H_2O$, ≥96%), cobalt(II) chloride hexahydrate ($CoCl_2 \cdot 6H_2O$, ≥98%), iron(III) chloride hexahydrate ($FeCl_3 \cdot 6H_2O$, ≥98%), *N*,*N*-dimethylformamide ($HCON(CH_3)_2$, ≥99.8%), ethanol (C_2H_5OH, HPLC grade), GO solution in water (1 wt.%, standard graphene), potassium hydroxide (KOH flake, ≥93%), and sulfuric acid (H_2SO_4, ≥98%) were obtained from Daejung Chemicals, South Korea.

S2. Characterization techniques

The crystalline structure and phase of the prepared materials were analyzed using X-ray diffraction analysis (XRD, Bruker D8 Advance A25 diffractometer, Germany). Raman spectra were recorded in a Raman imaging microscope with a 532-nm continuous laser (DXR2xi, Thermo Scientific). The surface structure and elemental composition were examined using field-emission scanning electron microscopy (FESEM, TESCAN, CLARA, Czech Republic) equipped with energy-dispersive spectroscopy (EDS, Ultim Max by Oxford) and high-resolution transmission electron microscopy (HRTEM, JEM-2100F, JEOL) with an acceleration voltage of 200 kV. High-angle annular dark-field scanning transmission electron microscopy (HAADF-STEM) and the corresponding EDS mapping were obtained with an ultrahigh-resolution double Cs probe-corrected transmission electron microscope (Spectra Ultra S/TEM, Thermo Fisher) operated at 300 kV. The chemical state of the prepared materials was studied via X-ray photoelectron spectroscopy (XPS, Nexsa G2, Thermo Scientific). The precise metal ratio in composites was determined using an inductively coupled plasma optical emission spectrometer (ICP-OES, PerkinElmer, Optima 8300DV).

S3. Electrochemical analyses

Electrochemical assessments were performed across three distinct pH environments: 1.0 M KOH, 0.5 M H_2SO_4, and 0.1 M $KClO_4$, utilizing a half-cell configuration on a CHI708E electrochemical analyzer. The experimental setup involved the employment of reference electrodes, Ag/AgCl for acidic and neutral solutions, and Hg/HgO for basic solutions, along with a Pt-wire counter electrode and the synthesized catalyst loaded on to the carbon cloth (CC) as the working electrode. To prepare the catalyst ink for 1.0 mg of the synthesized sample, 100 µL of water, 100 µL of ethanol, and 20 µL of Nafion were added, followed by sonication for

30 min. Subsequently, the resulting catalyst ink was dropped onto a 1 cm × 1 cm-sized CC substrate and dried at 50°C for a few hours. The CC was immersed in 0.5 M H_2SO_4 for 24 h prior to the experiment to increase wettability of CC, followed by thorough rinses with water and absolute ethanol, and finally dried in a hot-air oven overnight. This systematic approach allowed for the systematic exploration of electrochemical properties across diverse pH levels, enabling a comprehensive evaluation of the catalytic performance of the synthesized sample under various environmental conditions.

Prior to conducting electrochemical examination, the assembled working electrode was activated by carrying out 200 consecutive CV scans at a scan rate of 50 mV s^{-1} in the respective electrolyte solution (**Figures SI.1** and **SI.2**). Linear sweep voltammetry (LSV) polarization data were measured at a scan rate of 5 mV/s. All measured potentials were converted to the reversible hydrogen electrode (RHE) scale, unless specified otherwise. Tafel slope values were determined using the Tafel equation $\eta = b \times \log(j/j_0)$, where η is overpotential, j_0 and j denote exchange current density and current density, respectively, and b represents the Tafel slope. Electrochemical impedance spectroscopy (EIS) data were obtained over a frequency range of 10^{-1}–10^5 Hz at a fixed potential. The double-layer capacitance (C_{dl}) value, extracted from cyclic voltammetry (CV) profiles measured in the non-Faradaic area at different scan rates, was utilized to evaluate the electrochemical active surface area (ECSA) of fabricated catalysts. Furthermore, their turnover frequency (TOF) values were measured using TOF = $j \times A/(n \times F \times S_a)$, where A is the area of the electrode, n refers to the number of electrons participated in reactions (two for HER and four for OER), F is the Faraday constant (~96,485.33 C/mol), and S_a represents the active surface sites of electrode materials. S_a was determined using the following formula: $S_a = Q_s/F$, where Q_s represents the surface charge density obtained by integrating the total charge from full CV profiles.

OWS electrolyzer tests were conducted in a membrane-less two-electrode compartment using three different electrolytes with a universal pH. For comparative analysis, tests were performed with a state-of-the-art electrolyzer employing the Pt/C||IrO_2 pair.

S4. In situ/operando electrochemical Raman probe studies

In situ electrochemical Raman spectroscopy was conducted utilizing a Raman electrochemical flow reactor connected to a CHI708E electrochemical analyzer. The flow reactor featured a three-electrode setup with Ag/AgCl, graphite rod, and catalyst-loaded CC as the reference, counter, and working electrodes, respectively. A Raman microscope (DXR3, Thermo Fisher Scientific) was used to analyze samples, providing comprehensive insights into reaction mechanisms and the presence of reactive intermediate species during HER in 0.5 H_2SO_4. Equipped with an Nd:YAG laser and a high-resolution objective lens, the microscope could record Raman spectra in the range of 200–2500 cm^{-1}. These spectra were collected at different applied potentials using a chronoamperometric technique.

S5. X-ray absorption (XAS) studies

The XAS studies was carry out at BL8, (Synchrotron Light Research Institute, SLRI, Thailand). All XAS spectra were recorded in fluorescence mode using a Vortex ME4 13-element silicon drift detector. The photon energy calibration was performed using derivative of foil Fe (at 7112 eV), Co (at 7709 eV) and Ni (at 8333 eV) for K-edge and Pd (at 3173 eV), Pt (at 11564 eV) for L3-edge. The Ru was calibrated using KCl standard compound at peak position at 2822.3eV for L3-edge.

All XAS data were averaged and normalized using the Demeter software package (version 0.9.18.2). The k2-weight spectra were Fourier transformed between 3 and 10 for all elements, where k represents the wave vector.

S6. Computational study

All calculations in this work were performed using the DFT method as implemented in the SIESTA package [1-3], employing Troullier–Martins norm-conserving pseudopotentials in the Kleinman–Bylander form, along with the gradient-corrected Perdew, Burke, and Ernzerhof (PBE) exchange-correlation functional. The Coulombic interaction was accounted for by considering the Hubbard U potential for all transition metal atoms. A localized molecular orbital basis set with double-zeta polarization (DZP) and a real mesh cutoff of 300 Ry were used to represent all atoms. Long-range dispersions were handled using the Grimme D2 dispersion correction term. Initial structures were optimized without constraints under three-dimensional periodic boundary conditions, using convergence criteria of 0.05 eV for energy and 0.05 Å for displacement. The Brillouin zone sampling was conducted using a cell with 50 k-point grids.

The optimized structures were validated as minima based on computed real vibrational frequencies through phonon calculations at the Γ-point, using the SIESTA package, with central finite differencing of the analytical first derivatives and a displacement of 0.04 Bohr. A cubic structure was used as input in the SIESTA code with two possible compositions for CoFeNiPtPdRu HEA, [$Co_8Fe_8Ni_8Pt_2Pd_4Ru_2$] k1, and [$Co_9Fe_7Ni_8Pt_2Pd_4Ru_2$] k1a. Various configurations were generated and optimized without constraints, and the lowest energy configurations were used for adsorption studies. The unit cell size is 6.4 Å X 6.4 Å X 12. 8 Å

considered for this work. Subsequently, H^+, OH^-, and H_2O were introduced into the cell, which is extended to 13 Å in c-direction one at a time at various metal sites, and the relative energy barriers were calculated for both configurations.

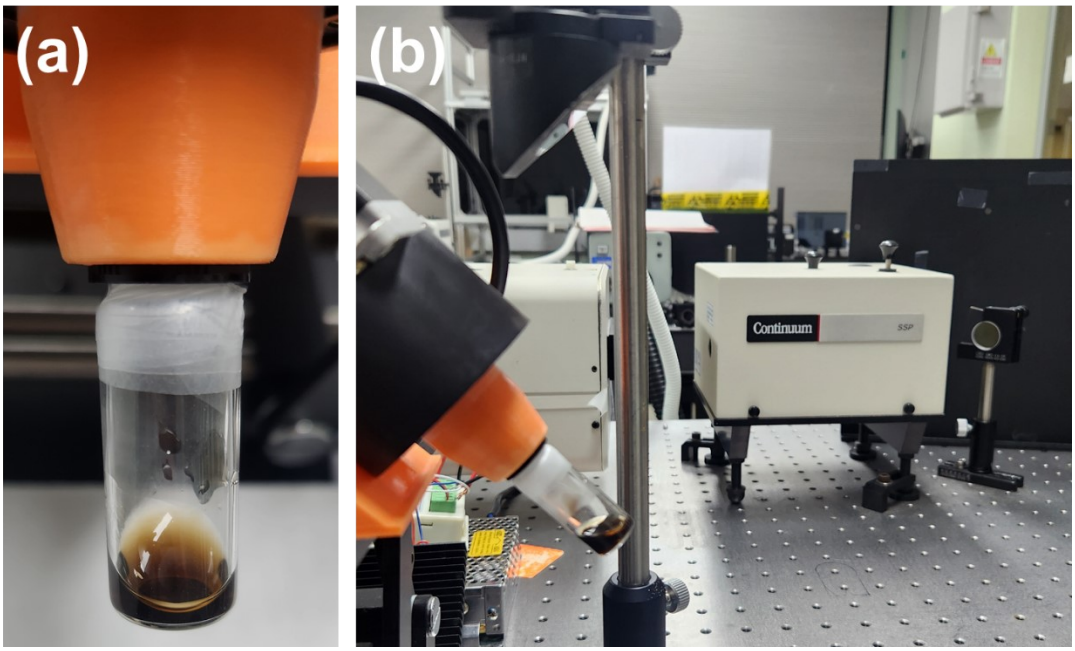

Figure S1. (a and b) Pictorial representation of PLIL rotating system-assisted synthesis of FeRuPtNiCoPd HEA–coordinated GO support (HESAC–HEA/GO) sample.

Table S1. ICP-OES elemental ratio for HESAC-HEA/GO-Fe^{2+}, and HESAC-HEA/GO-Fe^{3+}.

Atomic %	**Co**	**Fe**	**Ni**	**Pt**	**Pd**	**Ru**
HESAC-HEA/GO-Fe^{2+}	23.87	27.51	22.99	7.40	12.22	6.01
HESAC-HEA/GO-Fe^{3+}	33.99	21.41	14.49	8.92	13.71	7.48

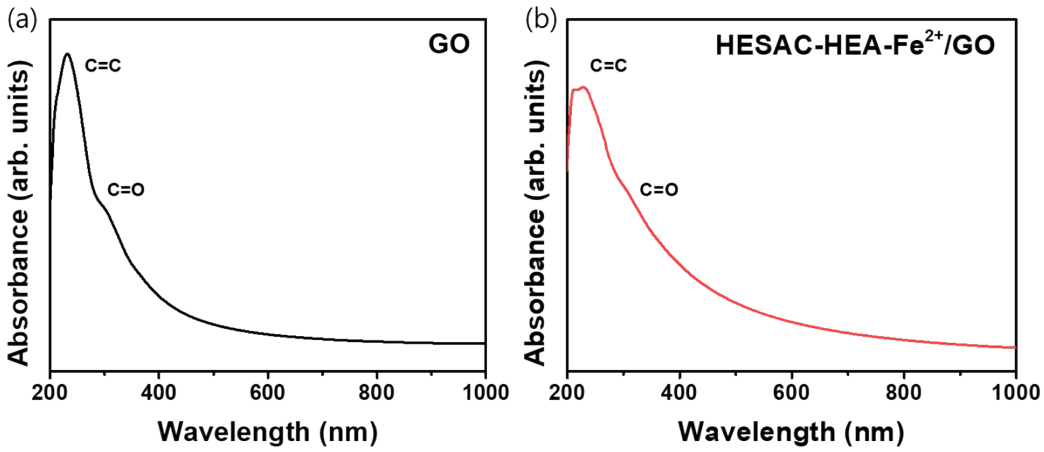

Figure S2. UV-vis spectra of pure GO and HESAC-HEA–Fe^{2+}/GO.

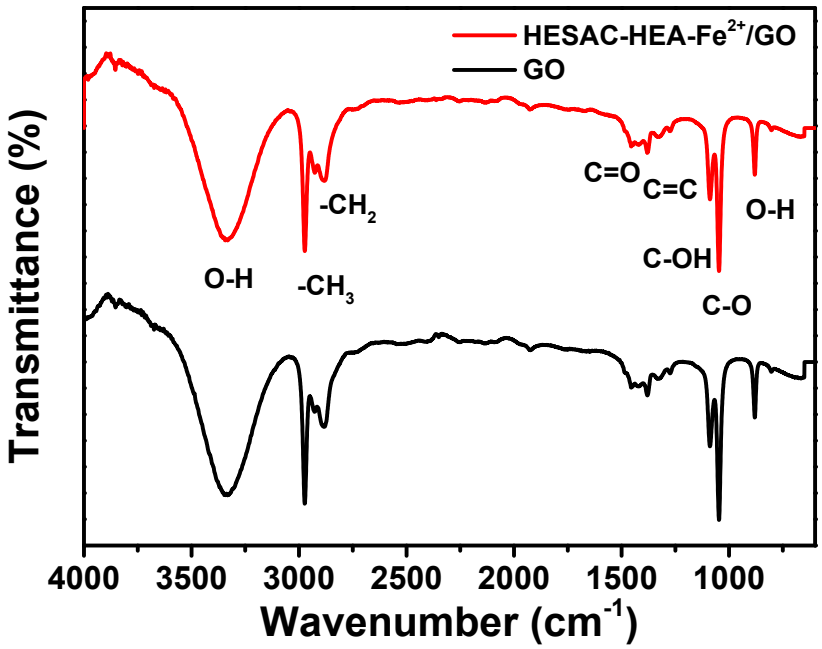

Figure S3. FTIR spectra of pure GO and HESAC-HEA–Fe^{2+}/GO.

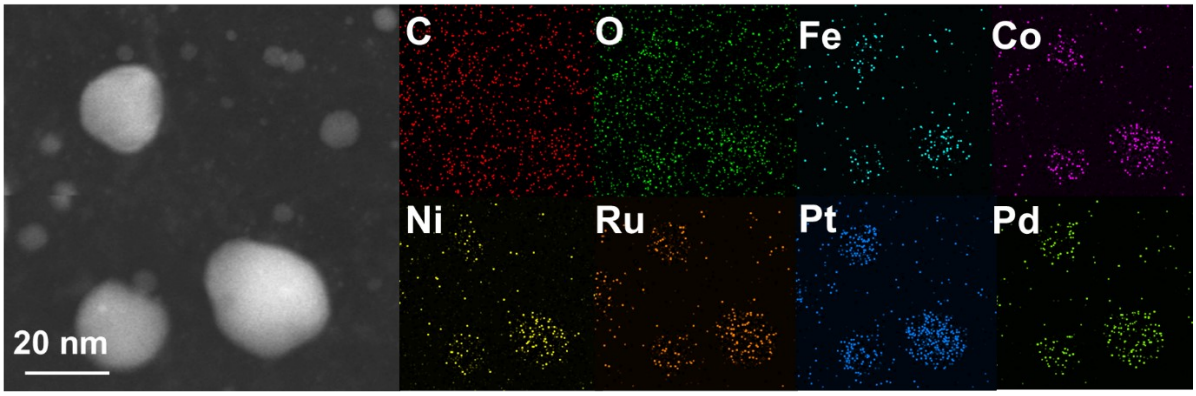

Figure S4. STEM-EDS mapping images of FeRuPtNiCoPd HESAC-HEA/GO-Fe^{2+} sample.

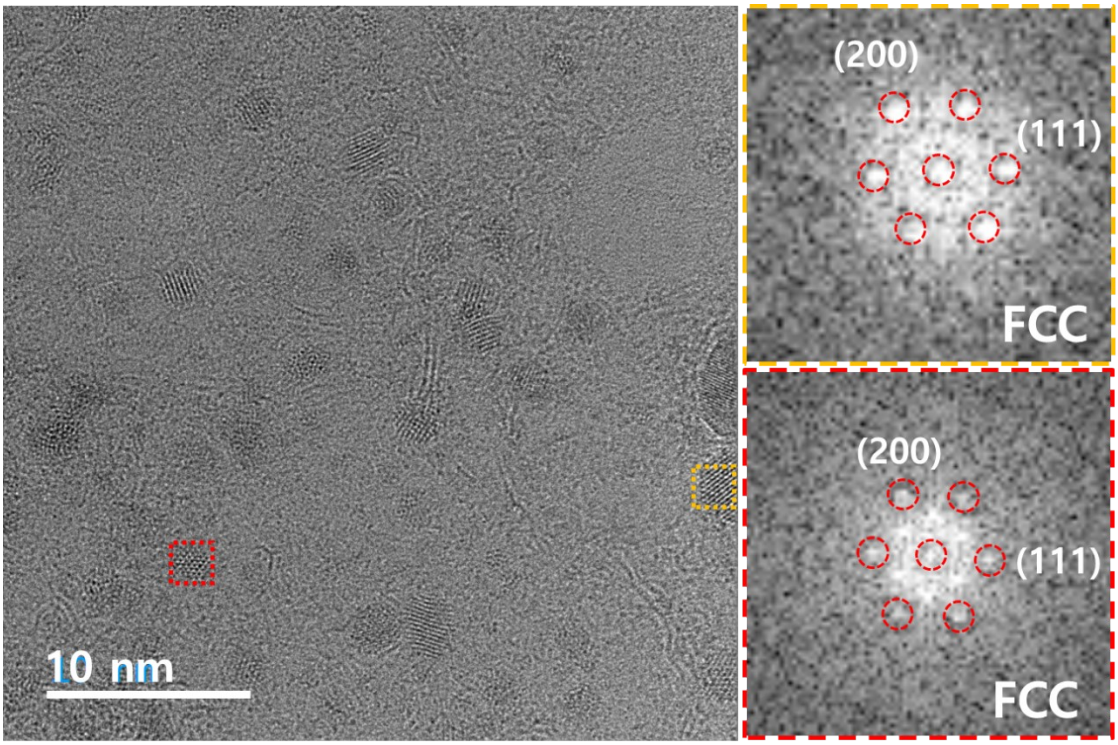

Figure S5. High-magnified HRTEM image of the HESAC–HEA/GO–Fe^{2+} sample with indexed lattice plane.

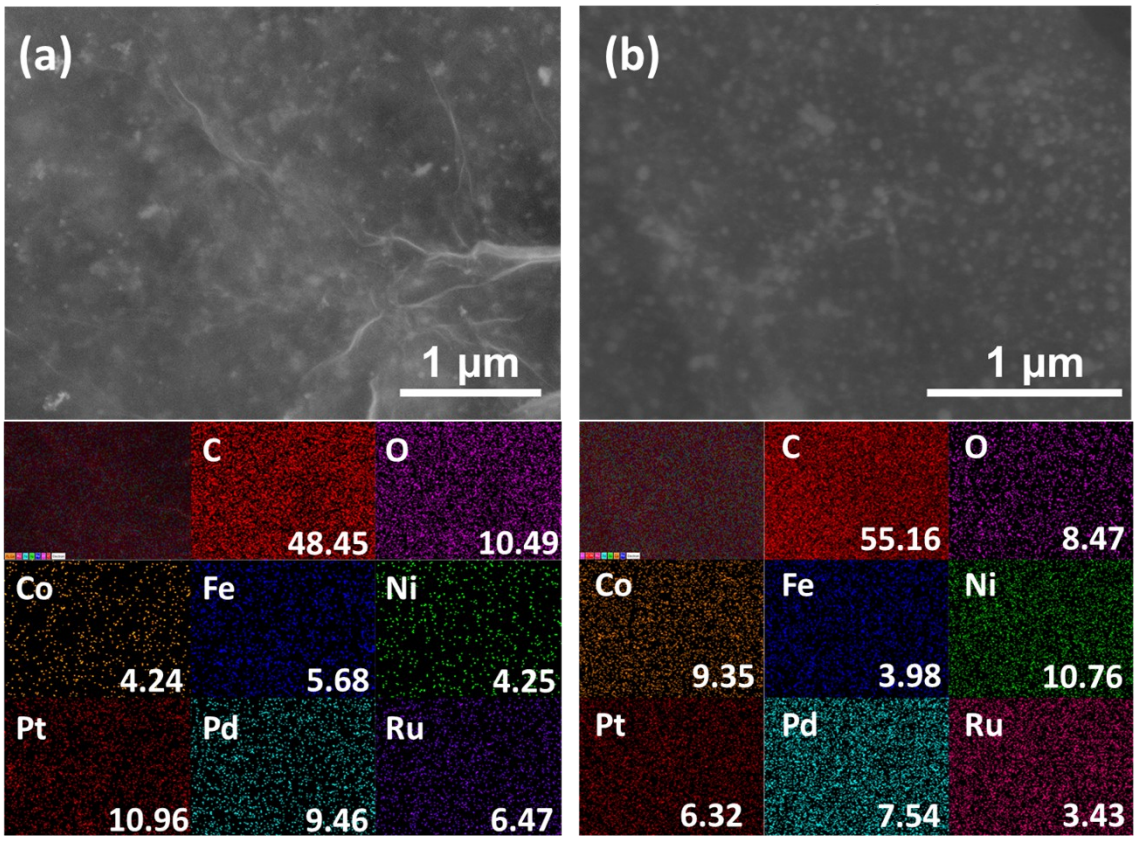

Figure S6. FESEM and EDS mapping of (a) HESAC-HEA/GO-Fe^{2+} and (b) HESAC-HEA/GO-Fe^{3+}.

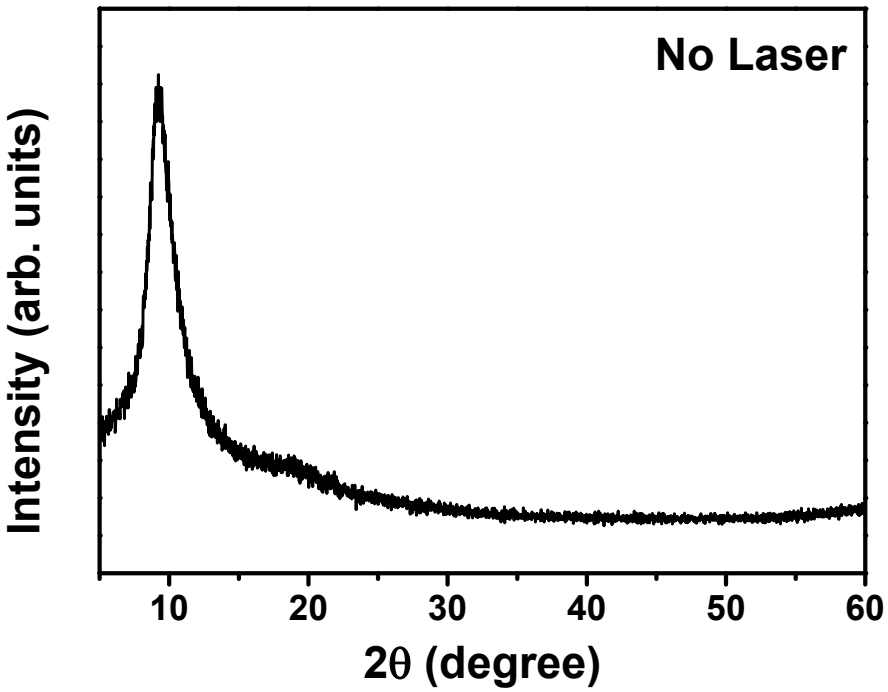

Figure S7. XRD pattern for the control experimental synthesis using the reaction mixture of metal salts with GO without applying laser irradiation.

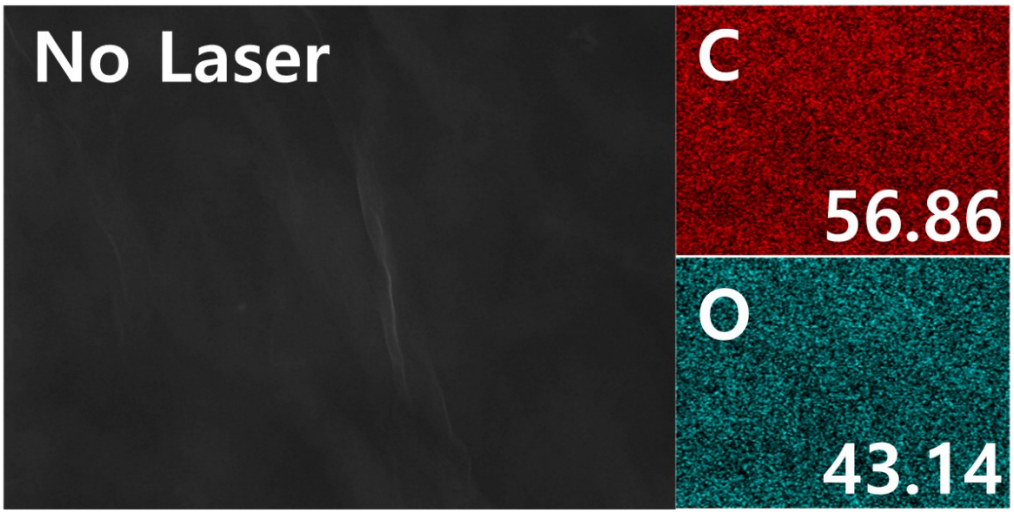

Figure S8. FESEM-EDS mapping for the control synthesis using the reaction mixture of metal salts with GO without applying laser irradiation.

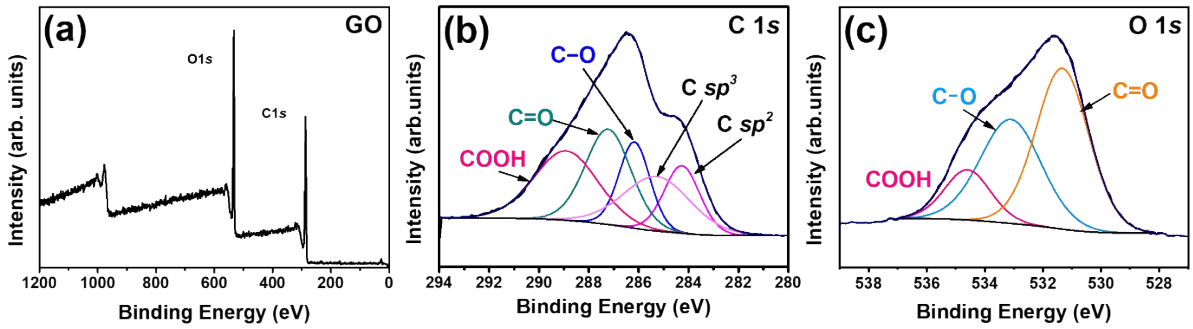

Figure S9. (a) XPS survey scan spectra of pure GO, (b) high resolution core-level C 1*s*, and (c) O 1*s*.

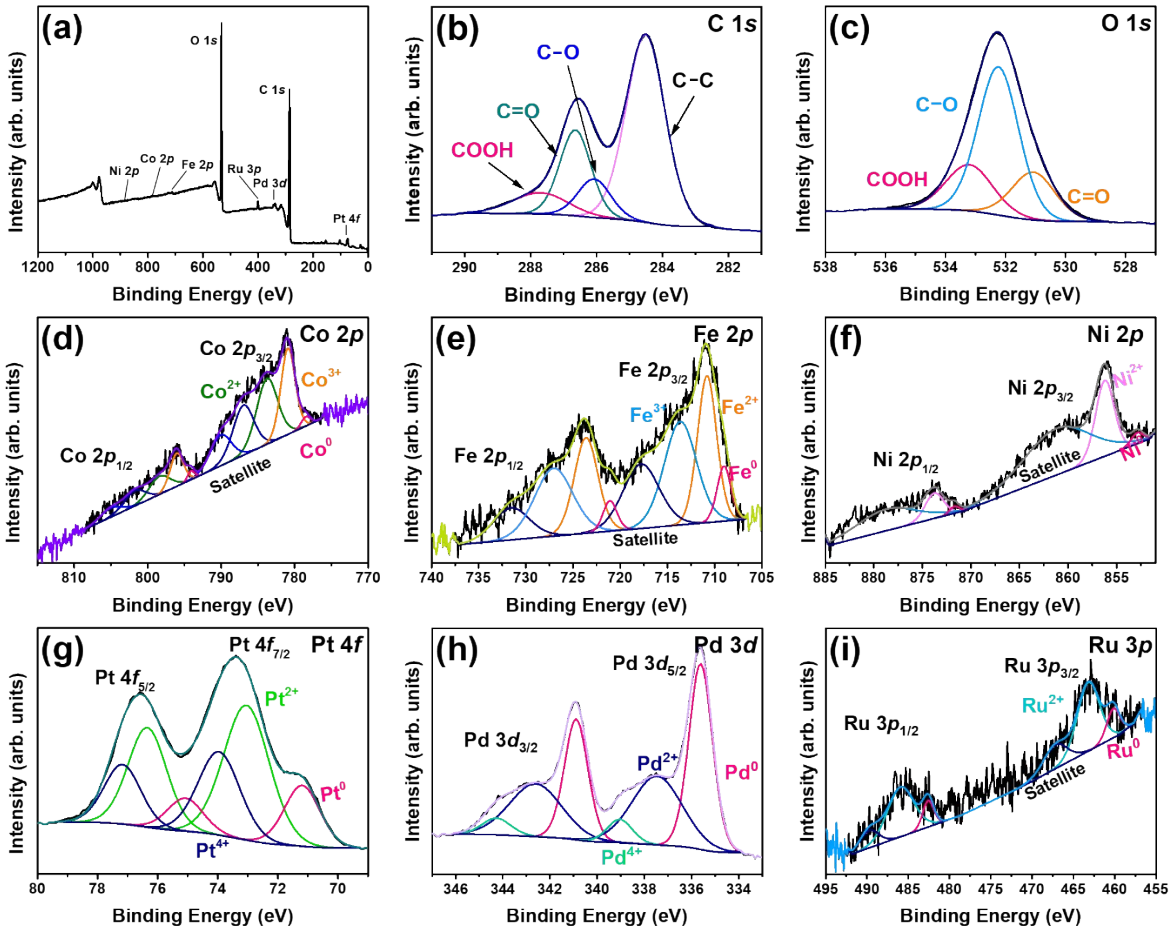

Figure S10. XPS spectra of the HESAC-HEA/GO-Fe^{3+} sample; (a) Full-survey, (b) C 1*s*, and (c) O 1*s*, (d) Co 2*p*, (e) Fe 2*p*, (f) Ni 2*p*, (g) Pt 4*f*, (h) Pd 3*d*, and (i) Ru 3*p*.

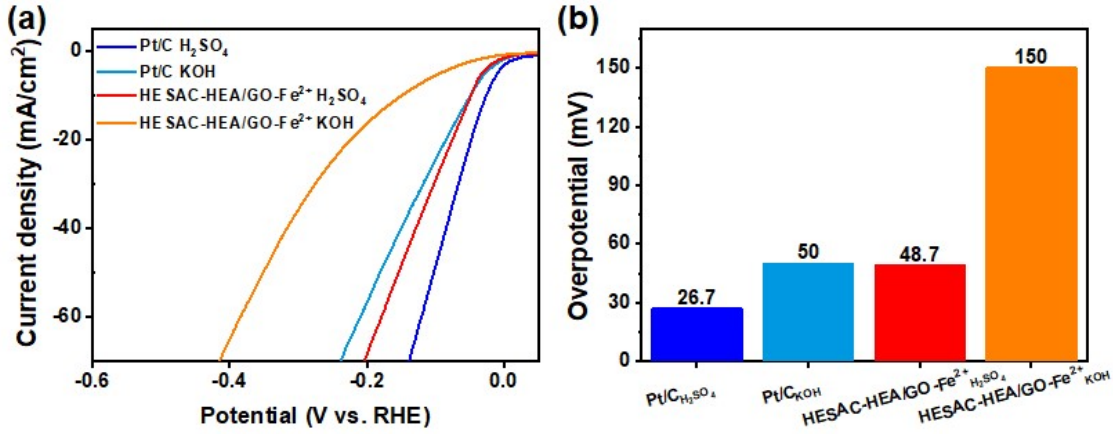

Figure S11. (a) HER polarization graphs of HESAC–HEA/GO–Fe^{2+} and commercial Pt/C in 0.5 M H_2SO_4 and 1.0 M KOH solutions at 5 mV/s, and (b) η at 10 mA/cm^2.

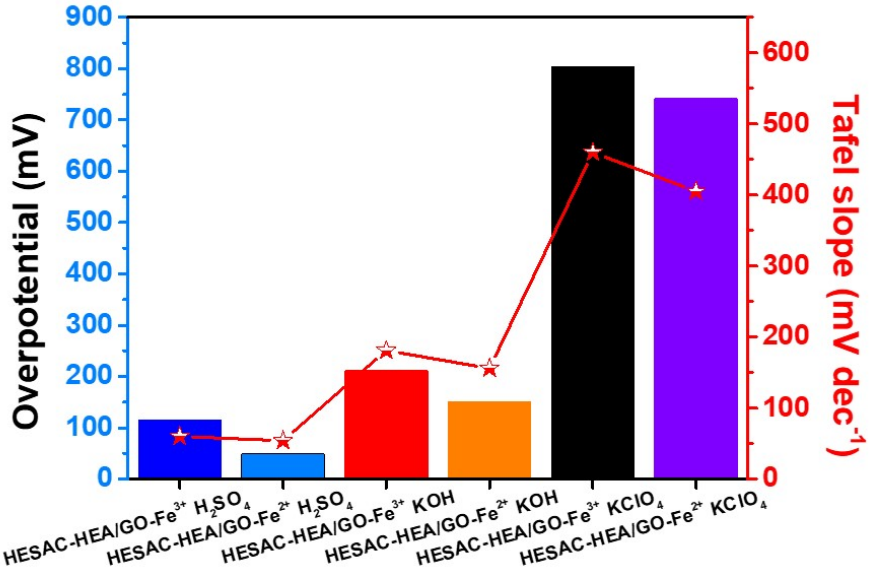

Figure S12. Comparison of HER activity with overpotential and Tafel slope of HESAC–HEA/GO–Fe^{2+} and HESAC–HEA/GO–Fe^{3+} electrocatalysts in different electrolyte media.

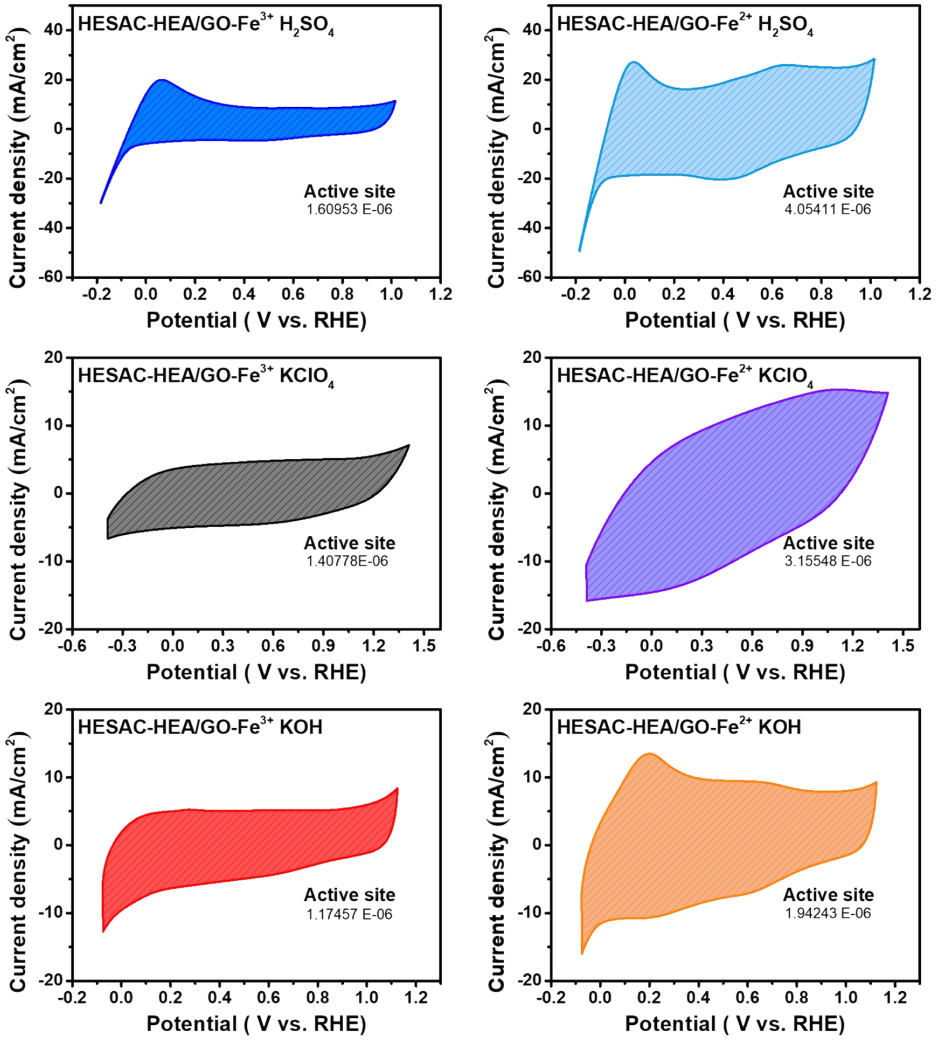

Figure S13. The CV profiles for the synthesized HESAC-HEA/GO-Fe^{2+} and HESAC-HEA/GO-Fe^{3+} catalysts obtained in the potential window of -0.1 to 1.2 V vs. RHE at 50 mV/s in different electrolytes.

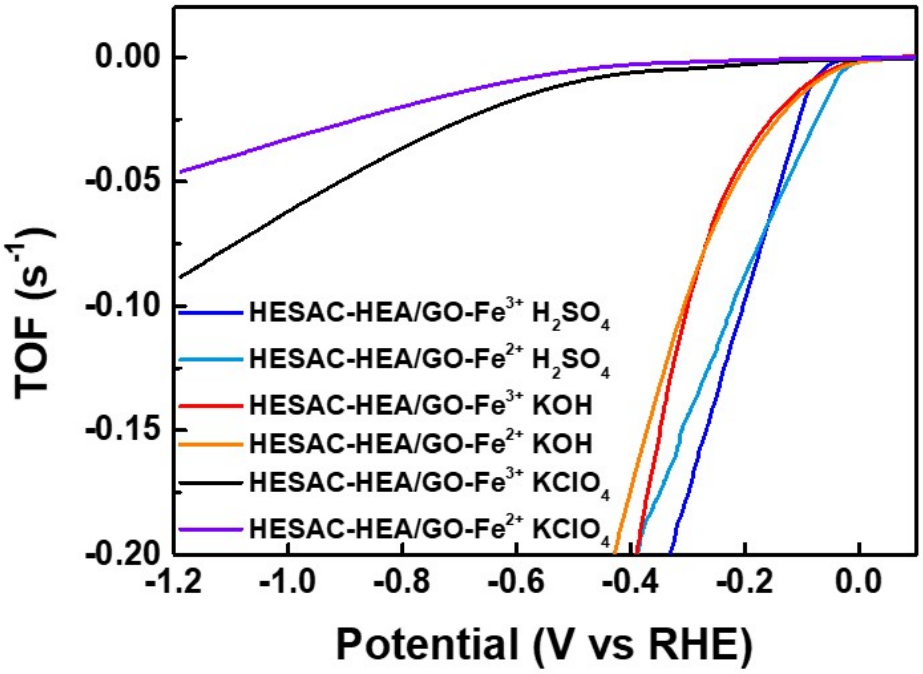

Figure S14. The evaluated TOF value at wide HER potential for the synthesized HESAC-HEA/GO-Fe^{2+} and HESAC-HEA/GO-Fe^{3+} in different electrolytes.

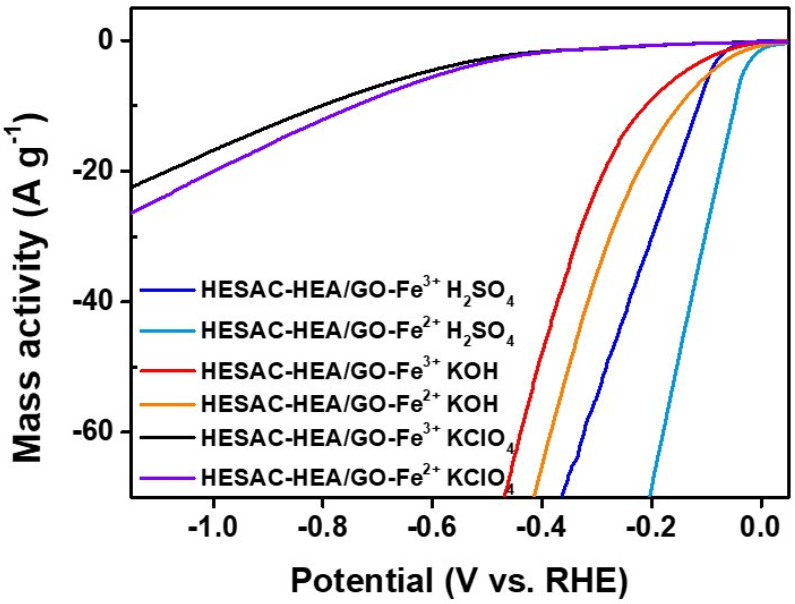

Figure S15. The evaluated mass activity at wide HER potential for the synthesized HESAC-HEA/GO-Fe^{2+} and HESAC-HEA/GO-Fe^{3+} in different electrolytes.

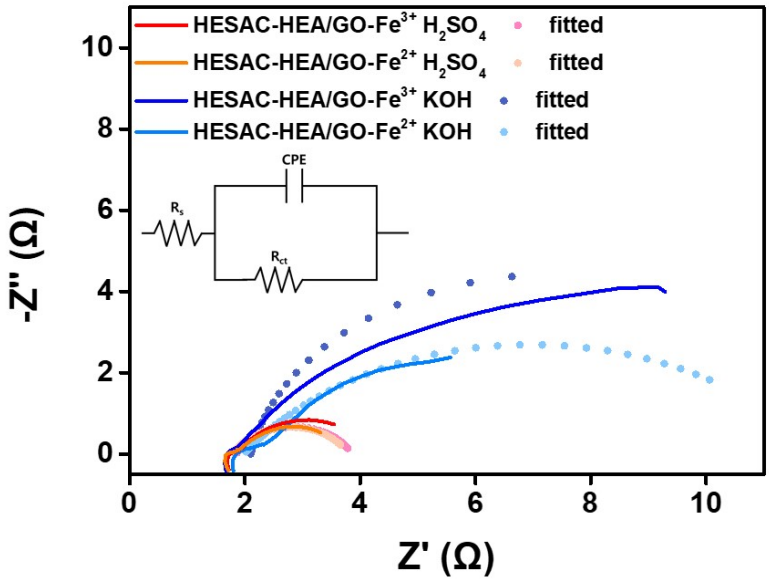

Figure S16. The fitted Nyquist impedance plot of HESAC-HEA/GO-Fe^{2+} and HESAC-HEA/GO-Fe^{3+} in different electrolytes measured at −0.136 V vs. RHE (Inset show fitted Randles equivalent circuit).

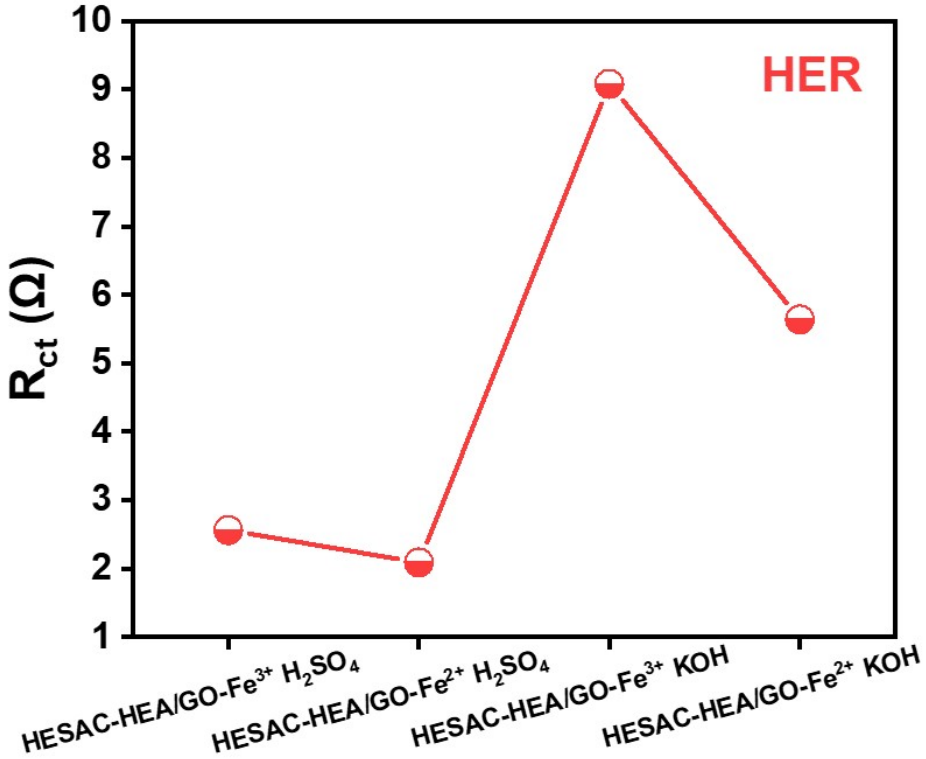

Figure S17. The extracted charge-transfer resistance (R_{ct}) value from the Nyquist impedance plot of HESAC-HEA/GO-Fe^{2+} and HESAC-HEA/GO-Fe^{3+} in different electrolytes measured at −0.136 V vs. RHE.

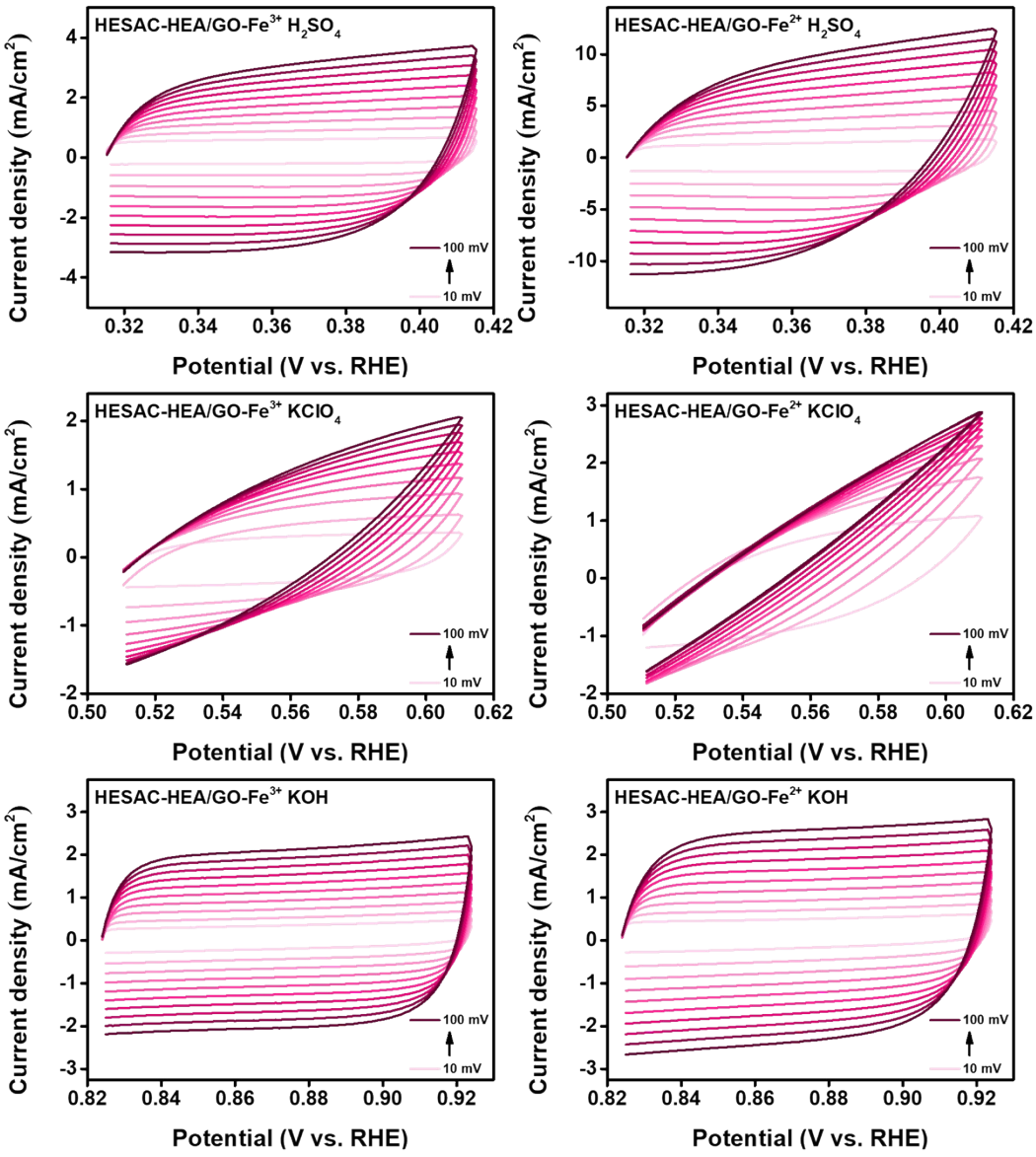

Figure S18. CV profiles of HESAC-HEA/GO-Fe^{2+} and HESAC-HEA/GO-Fe^{3+} catalysts measured in the non-Faradic portion in 0.5 M H_2SO_4, 1.0 M KOH, and 0.1 M $KClO_4$ electrolytes at different scan rate from 20-100 mV/s.

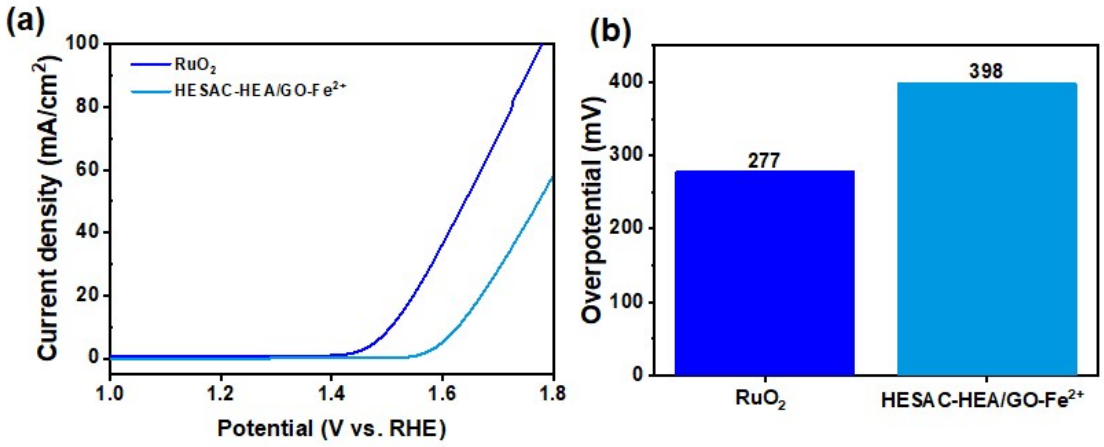

Figure S19. (a) OER polarization graphs of HESAC–HEA/GO–Fe^{2+} and commercial RuO_2 in 1.0 M KOH solution at 5 mV/s, and (b) η at 10 mA/cm^2.

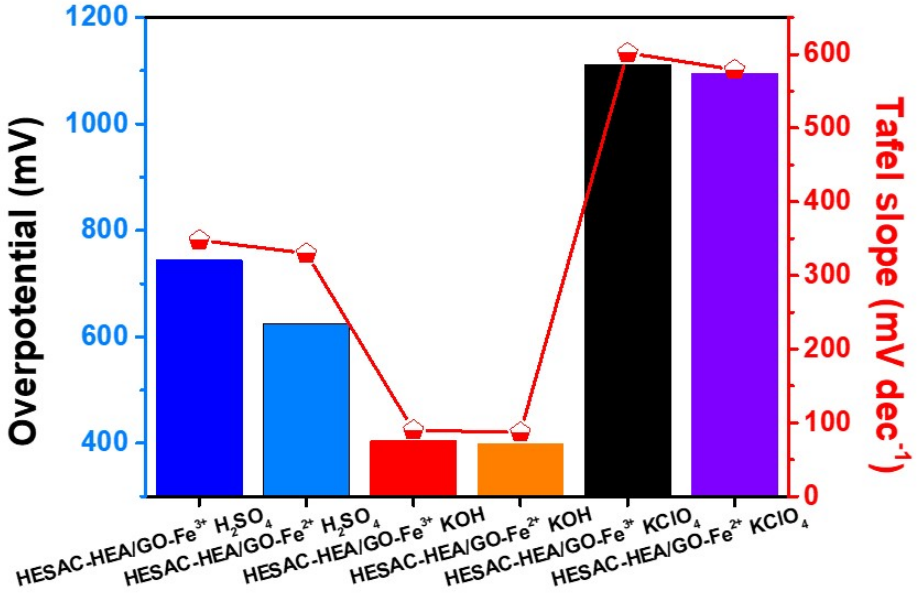

Figure S20. Comparison of OER activity with overpotential and Tafel slope of HESAC–HEA/GO–Fe^{2+} and HESAC–HEA/GO–Fe^{3+} electrocatalysts in different electrolyte media.

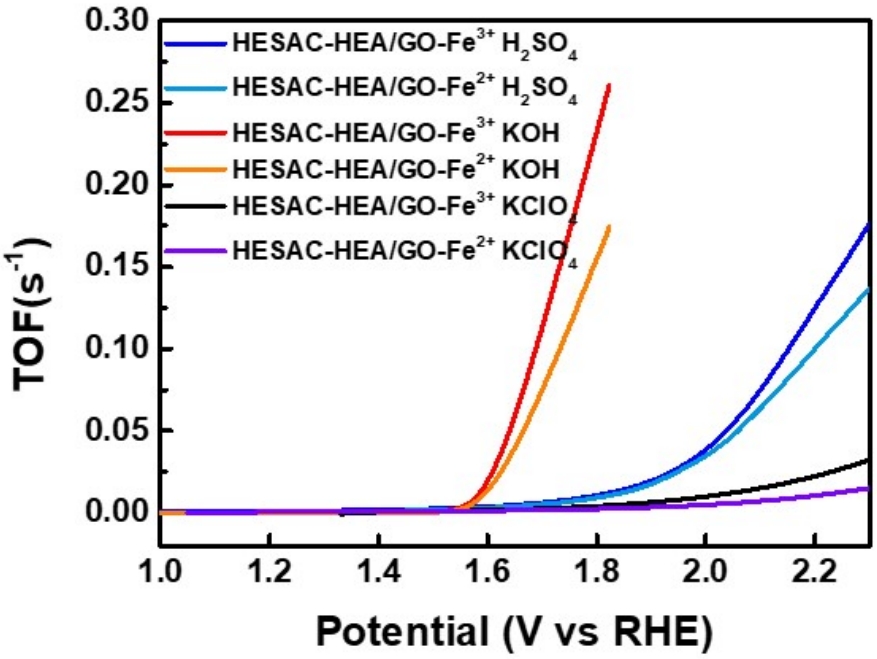

Figure S21. The evaluated TOF value at wide OER potential for the synthesized HESAC-HEA/GO-Fe^{2+} and HESAC-HEA/GO-Fe^{3+} in different electrolytes.

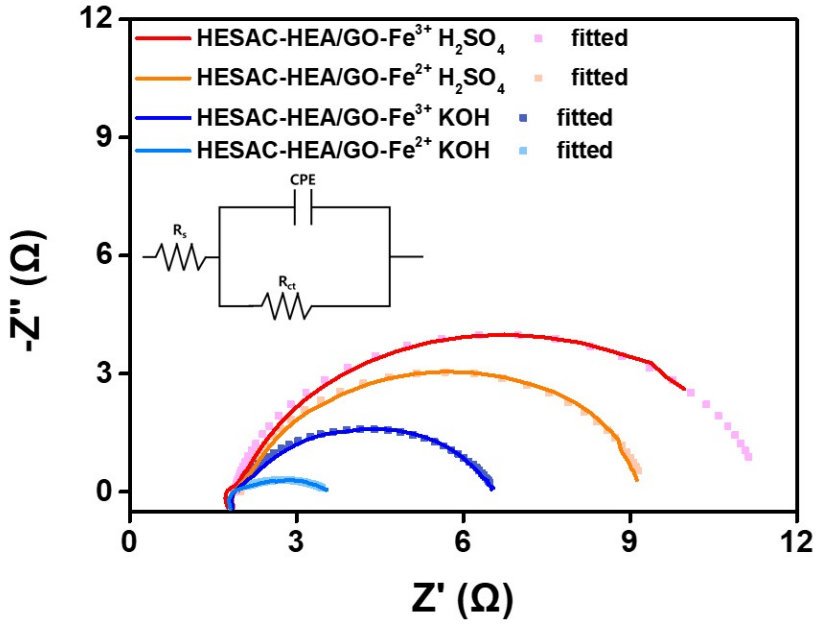

Figure S22. The fitted Nyquist impedance plot of HESAC-HEA/GO-Fe^{2+} and HESAC-HEA/GO-Fe^{3+} in different electrolytes measured at **−0.136 V vs. RHE** (Inset show fitted Randles equivalent circuit).

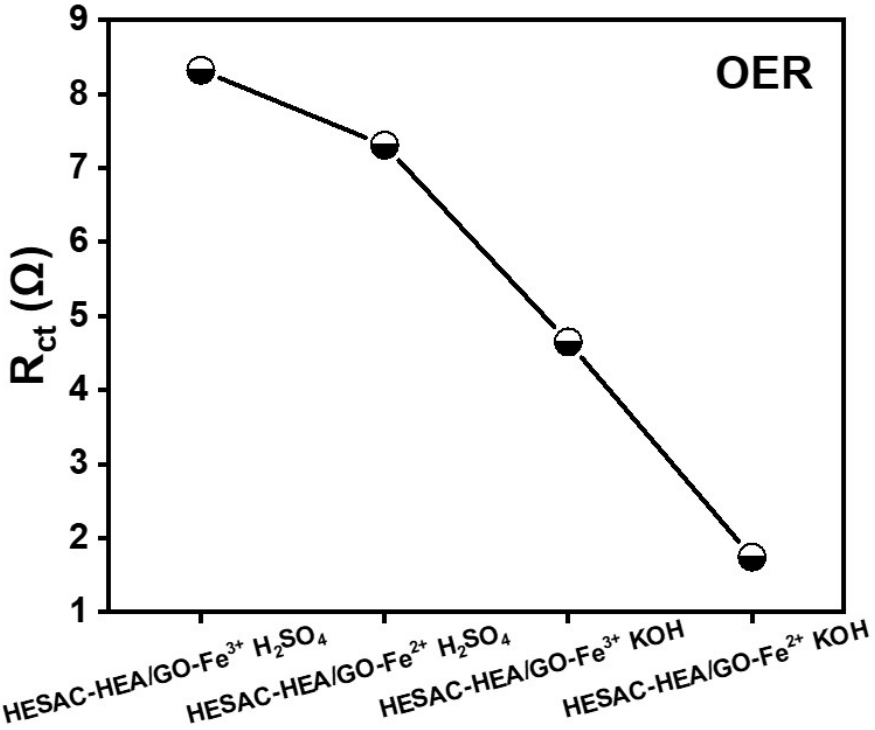

Figure S23. The extracted charge-transfer resistance (R_{ct}) value from the Nyquist impedance plot of HESAC-HEA/GO-Fe^{2+} and HESAC-HEA/GO-Fe^{3+} in different electrolytes measured at −0.136 V vs. RHE.

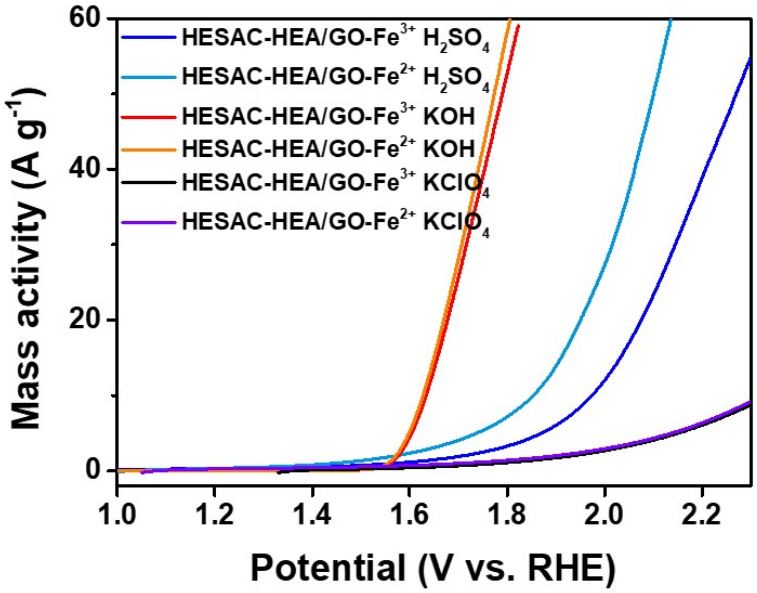

Figure S24. The evaluated mass activity at wide OER potential for the synthesized HESAC-HEA/GO-Fe^{2+} and HESAC-HEA/GO-Fe^{3+} in different electrolytes.

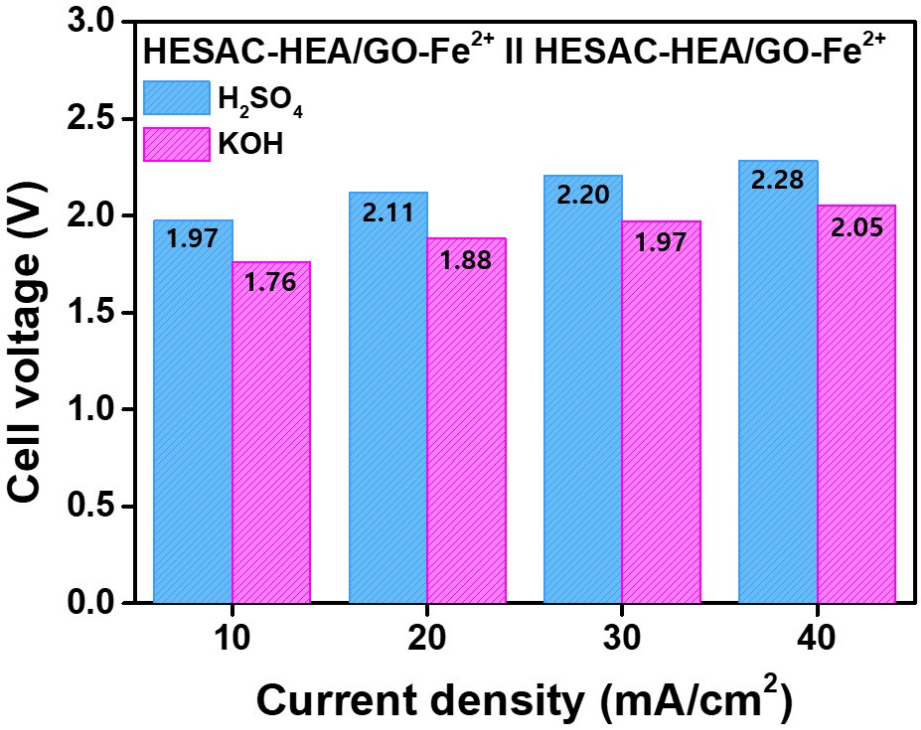

Figure S25. The cell voltage required to deliver various current density for the fabricated HESAC–HEA/GO–Fe^{2+}‖HESAC–HEA/GO–Fe^{2+} electrolyzer in 1.0 M KOH and 0.5 M H_2SO_4 electrolytes.

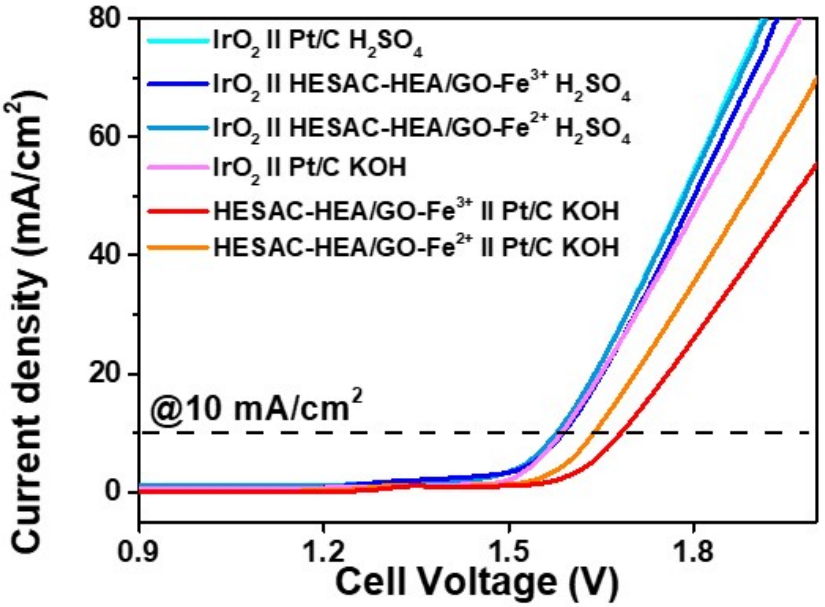

Figure S26. Polarization curves of the fabricated IrO_2 ‖ Pt/C, IrO_2 ‖ HESAC-HEA/GO-Fe^{2+}, and IrO_2 ‖ HESAC-HEA/GO-Fe^{3+} in 0.5 M H_2SO_4 and 1.0 M KOH electrolytes.

Figure S27. Pictorial representation of the fabricated two-electrode membrane-less electrolyzer.

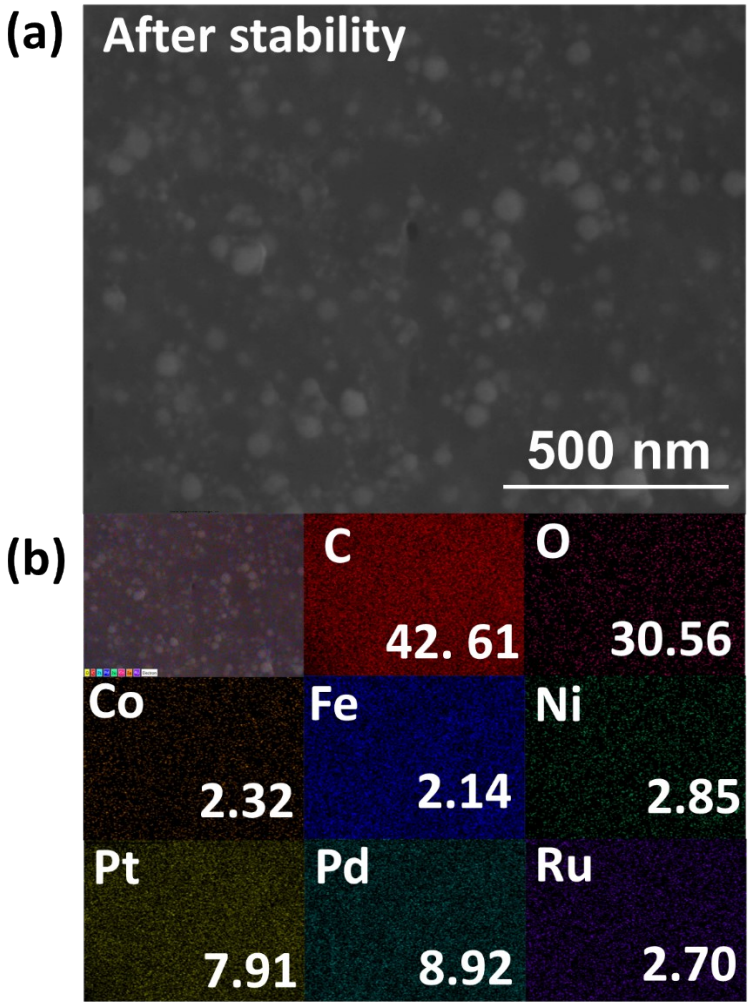

Figure S28. (a) FESEM image and (b) EDS mapping of analysis of HESAC–HEA/GO–Fe^{2+} anode electrode fabricated on CC substrate after long-term OWS test.

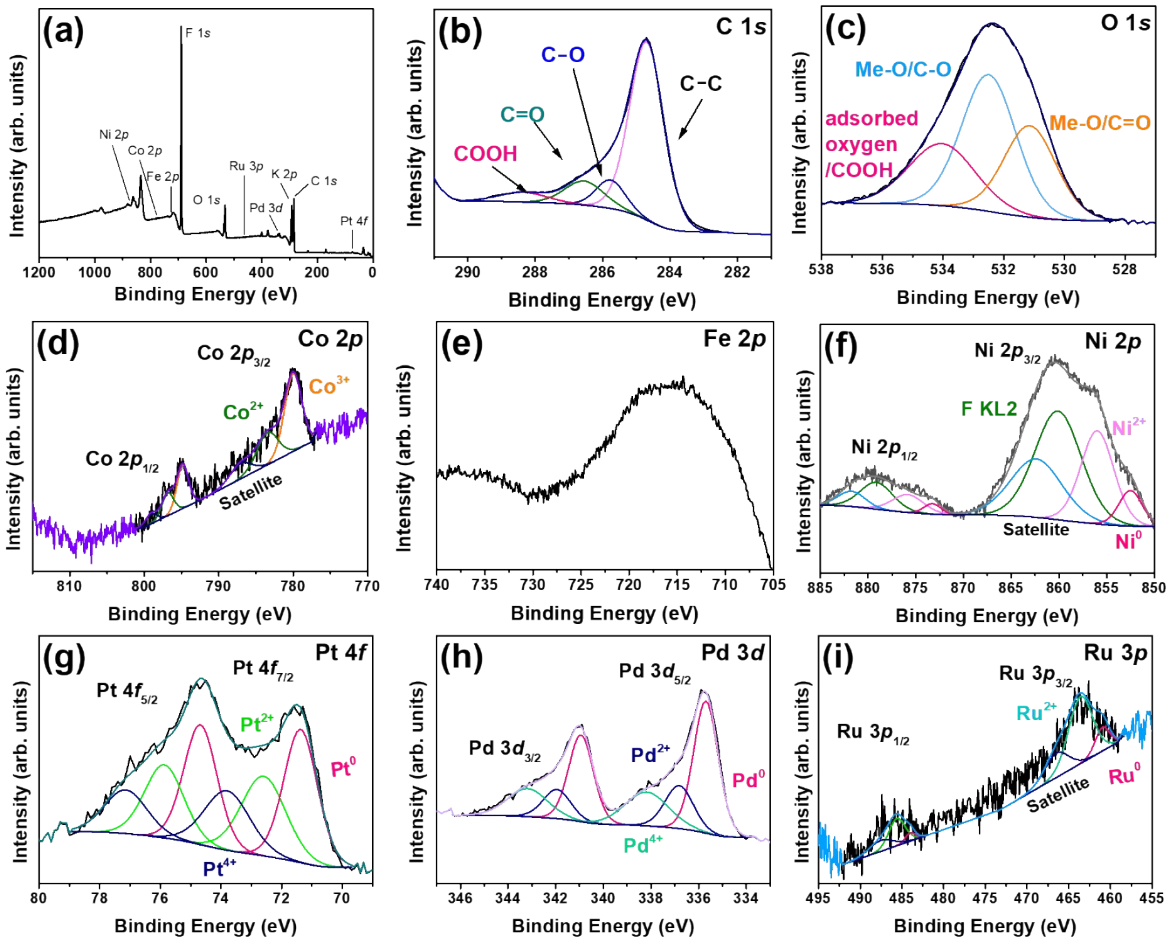

Figure S29. XPS spectra of the HESAC–HEA/GO–Fe^{2+} anode electrode fabricated on CC substrate after long-term OWS test: (a) full-survey, (b) C 1*s*, (c) O 1*s*, (d) Co 2*p*, (e) Fe 2*p*, (f) Ni 2*p*, (g) Pt 4*f*, (h) Pd 3*d*, and (i) Ru 3*p*.

Table S2. HER of the fabricated HESAC–HEA/GO–Fe^{2+} sample compared with the earlier reported HEA-based electrocatalysts.

No.	Catalysts	Synthesis routes	Over pote ntial (mV)	Tafel slope (mV dec^{-1})	Electrolyte	Ref.

			@ 10 mA cm^{-2}			
1	PtRhNiFeCu/C	Chemical reduction	13	29.8	1.0 M KOH	[4]
2	PdFeCoNiCu/C	Chemical reduction	18	39	1.0 M KOH	[5]
3	IrPdPtRhRu	One-pot polyol process	35.5	-	1.0 M KOH	[6]
4	CoCrFeNi	Arc-melted	60	62	0.5 M H_2SO_4	[7]
5	NiCoFePtRh	Thermal reduction	27	30.1	0.5 M H_2SO_4	[8]
6	CoCrFeNiAl	Mechanical alloying and spark plasma sintering	73	39.7	0.5 M H_2SO_4	[9]
7	PdPtCuNiP	Thermal reduction	32	37.4	1.0 M KOH	[10]
8	PdPtCuNiP	Thermal reduction	62	44.6	0.5 M H_2SO_4	[10]
9	$CoCuFeNiMnMo_{1.5}$	Mechanical alloying	275	125	1.0 M KOH	[11]
10	$Pt_{34}Fe_5Ni_{20}Cu_{31}Mo_9Ru$	Chemical reduction	20	27	1.0 M KOH	[12]
11	NiFeCoCuTi	Dealloying	48.7	57.0	1.0 M KOH	[13]
12	FeCoNiCuMoB/NF	Pulsed DC reactive magnetron sputtering	26	53.1	1.0 M KOH	[14]
13	CrFeNiCopZnS	Thermal reaction with CS_2	49	235	1.0 M KOH	[15]
14	FeCoCrMnNi	Pulsed electrodeposition	168	180	1.0 M KOH	[16]
15	RuPdIrPtAu/CNT	PLIL	30.7	71.07	1.0 M KOH	[17]
16	$PtRu_{2.9}Fe_{0.15}Co_{1.5}Ni_{1.3}$	$NaBH_4$ chemical reduction	11.8	41.0	1.0 M KOH	[18]
17	$Pt_{26}Ir_7Fe_{13}Co_{22}Ni_{32}$	Oleylamine chemical reduction	26	44.5	1.0 M KOH	[19]
18	PdCeMoCuRu	N-oleyl-1,3-	12.8	30.4	0.5 M H_2SO_4	[20]

		propanediamine chemical reduction				
19	FeCoNiMnRuLa/CNT	Thermal reduction	50	116.9	1.0 M KOH	[21]
20	Pt-NiFeCoCuCr double hydroxide (Pt/HE-LDH)	Hydrothermal	42	42	0.5 M H_2SO_4	[22]
21	HESAC–HEA/GO–Fe^{2+}	PLIL	49	54	0.5 M H_2SO_4	This work

Table S3. OER of the fabricated HESAC–HEA/GO–Fe^{2+} sample compared with the earlier reported HEA-based electrocatalysts.

No.	**Catalysts**	**Synthesis routes**	**Overpotential (mV) @ 10 mA cm^{-2}**	**Tafel slope (mV dec^{-1})**	**Electrolyte**	**Ref.**
1	Np-AlNiCoFeMo	Induction-melting under the Ar protection	240	46	1.0 M KOH	[23]
2	IrFeCoNiCu	Microwave-assisted shock synthesis	302	58	0.1 M $HClO_4$	[24]
3	FeNiMoCrAl	Sputter-deposited	220	27.3	1.0 M KOH	[25]
4	Porous CoCrFeNiMo-20	Microwave sintering.	220	59.0	1.0 M KOH	[26]
5	FeCoNiCrMn thin films	Magnetron sputtering	282	100	1.0 M KOH	[27]
6	Al-Ni-Co-Ir-Mo	Induction-melting under the Ar protection	233	55.2	0.5 M H_2SO_4	[28]
7	CrMnFeCoNi	Low-temperature solution-based approach	265	37.9	1.0 M KOH	[29]
8	FeCoNiMo HEA/C	Solvothermal and high	250	48.02	1.0 M KOH	[30]

		temperature reaction				
9	CoCuFeNiMnMo	Mechanical alloying	375 ± 15	61	1.0 M KOH	[11]
10	FeCoNiCiMn-NP(HEA-950)	Solvothermal – high temperature reaction	197	55	1.0 M KOH	[31]
11	NiFeCoCuTi	Dealloying	264.2	67.7	1.0 M KOH	[13]
12	FeCoNiCuMoB/NF	Pulsed DC reactive magnetron sputtering	201	41.3	1.0 M KOH	[14]
13	CrFeNiCopZnS	Thermal reaction with CS_2	370	63	1.0 M KOH	[15]
14	FeCoCrMnNi	Pulsed electrodeposition	231	66	1.0 M KOH	[16]
15	RuPdIrPtAu/CNT	PLIL	330	91.11	1.0 M KOH	[17]
16	$Pt_{26}Ir_7Fe_{13}Co_{22}Ni_{32}$	Oleylamine chemical reduction	197	37.7	1.0 M KOH	[19]
17	FeCoNiCuCr	Ultrafast CTS method	272	84.9	1.0 M KOH	[32]
18	PtNiCuMnMo	Vacuum arc melting	250	124	1.0 M KOH	[33]
19	Ir_2RuCoCuNi	SD-TDR method	264	47	1.0 M KOH	[34]
20	FeCoNiMnRuLa/CNT	Thermal reduction	281	47.5	1.0 M KOH	[21]
21	HESAC–HEA/GO–Fe^{2+}	PLIL	398	87	1.0 M KOH	This work

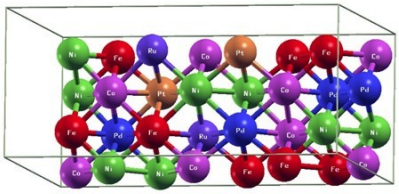

K1

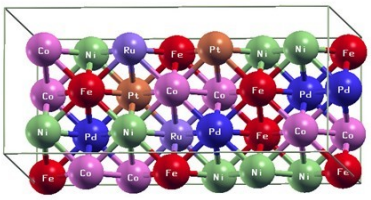

K2

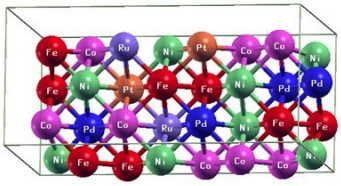

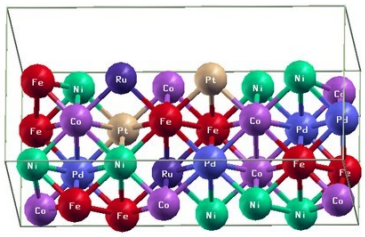

k4

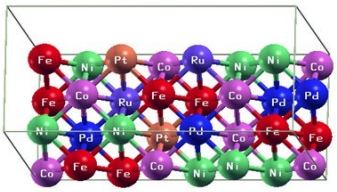

k5

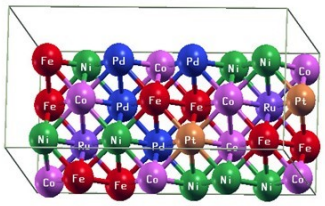

k6

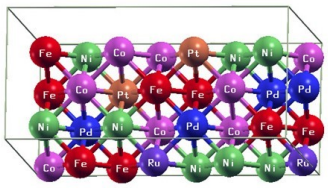

k7

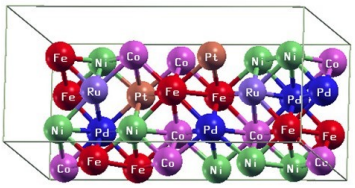

k8

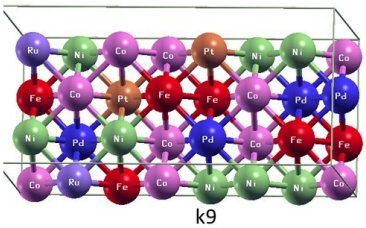

k9

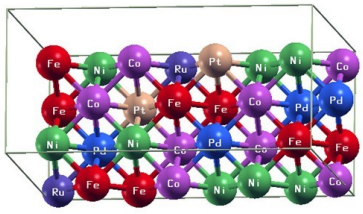

k10

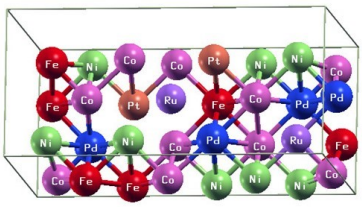

k11

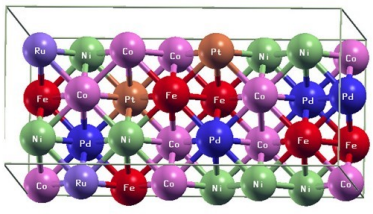

k12

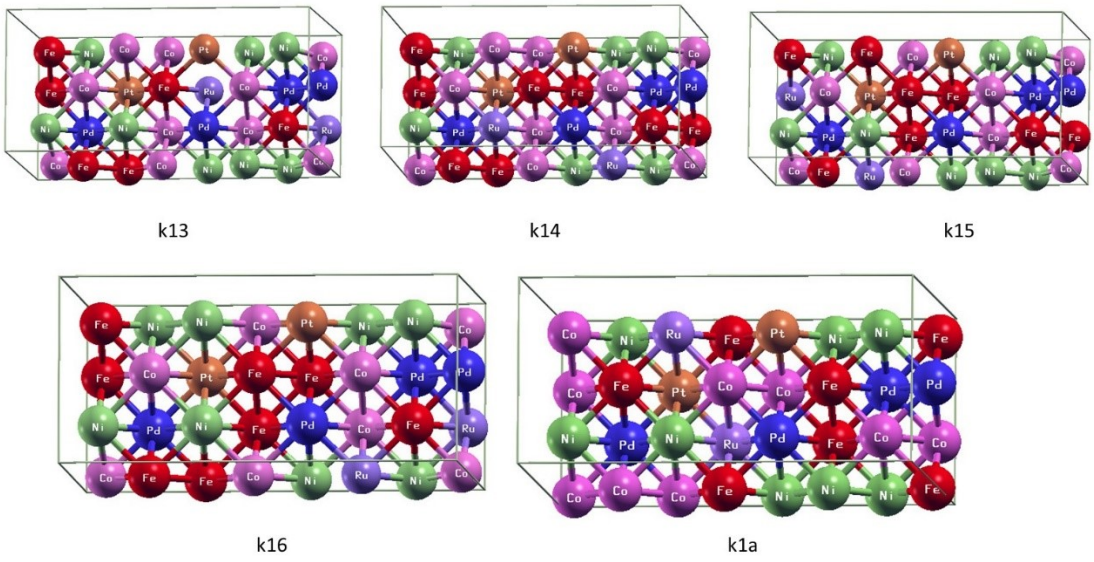

Figure S30. Various configuration of CoFeNiPtPdRu HEA optimized in this work. From this lowest energy k1 and k1a configuration used for catalytic adsorption studies.

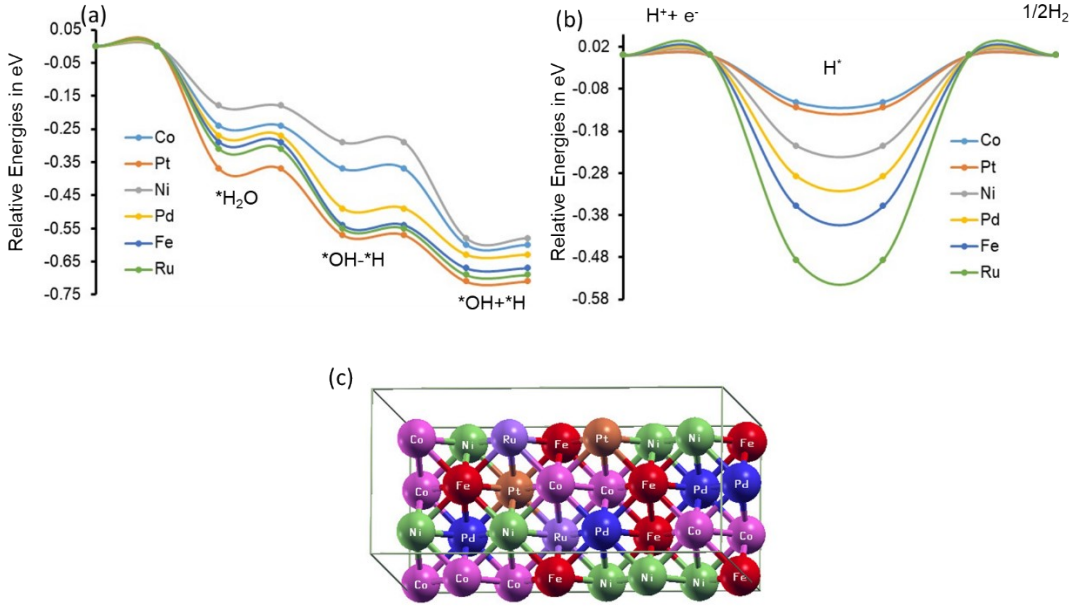

Figure S31. (a) Reaction energy profile for water dissociation, (b) H-adsorption on various catalytic sites of CoFeNiPtPdRu, k1a HEA surface, and (c) the k1a atomic configuration of HEA.

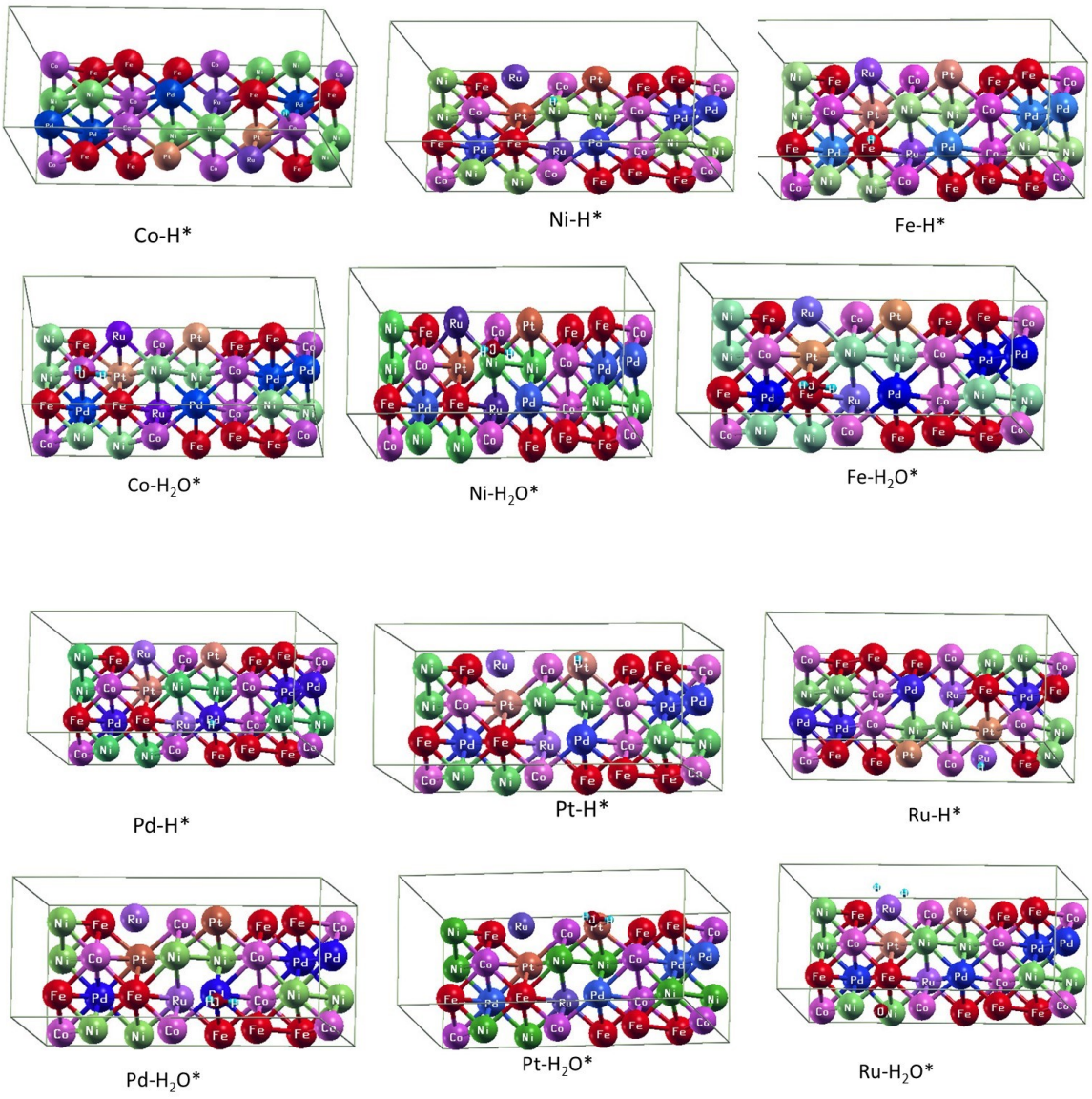

Figure S32. Optimized atomic configuration of all catalytic sites for k1 model.

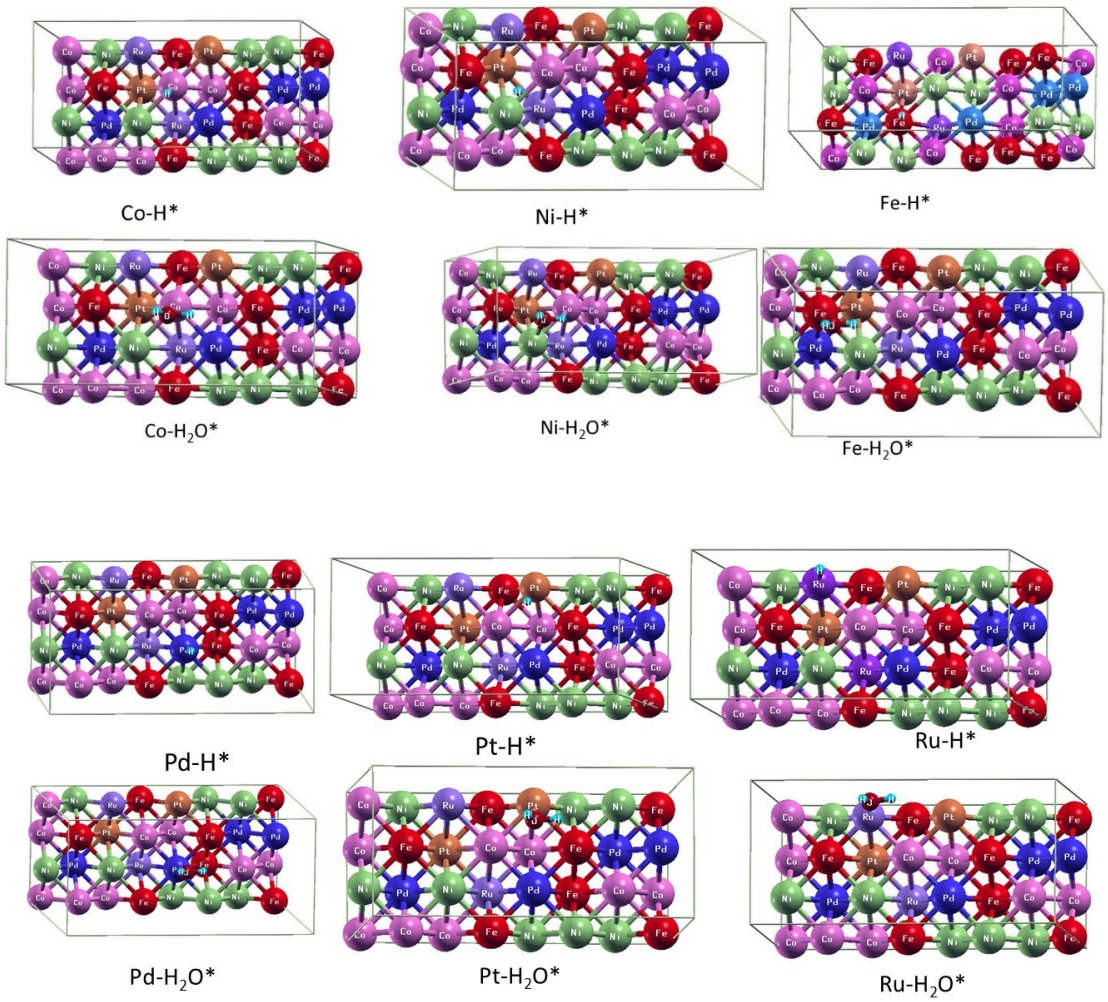

Figure S33. Optimized atomic configuration of all catalytic sites for k1a model.

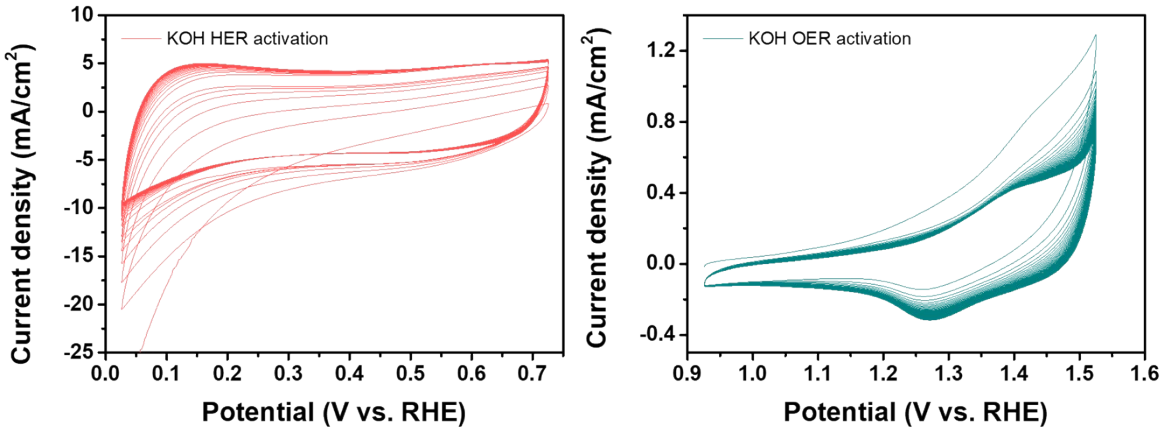

Figure SI.1. Pre-electrochemical activation of the fabricated HESAC–HEA/GO–Fe^{2+} electrode on carbon cloth substrate through 200 continuous CV sweeps for HER and OER at a 50 mV s^{-1} in 1.0-M KOH

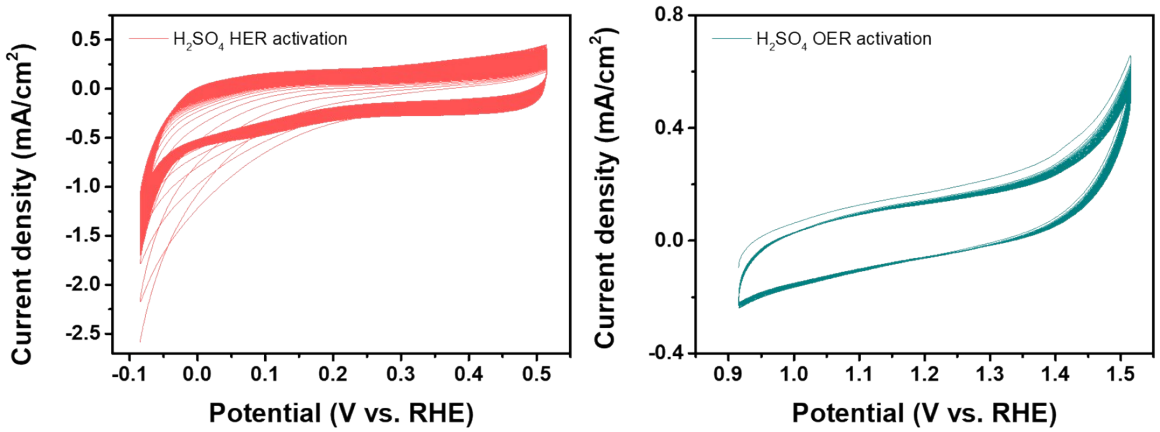

Figure SI.2. Pre-electrochemical activation of the fabricated HESAC–HEA/GO–Fe^{2+} electrode on carbon cloth substrate through 200 continuous CV sweeps for HER and OER at a 50 mV s^{-1} in 0.5-M H_2SO_4.

References

[1] E. Artacho, D. Sánchez-Portal, P. Ordejón, A. García, J.M. Soler, Linear-Scaling ab-initio Calculations for Large and Complex Systems, physica status solidi (b), 215 (1999) 809-817.

[2] E. Artacho, E. Anglada, O. Diéguez, J.D. Gale, A. García, J. Junquera, R.M. Martin, P. Ordejón, J.M. Pruneda, D. Sánchez-Portal, J.M. Soler, The SIESTA method; developments and applicability, Journal of Physics: Condensed Matter, 20 (2008) 064208.

[3] M.S. José, A. Emilio, D.G. Julian, G. Alberto, J. Javier, O. Pablo, S.-P. Daniel, The SIESTA method for ab initio order-N materials simulation, Journal of Physics: Condensed Matter, 14 (2002) 2745.

[4] Z. Hu, K. Chen, Y. Zhu, B. Liu, J. Shen, Synergistic Effects of PtRhNiFeCu High Entropy Alloy Nanocatalyst for Hydrogen Evolution and Oxygen Reduction Reactions, Small, n/a (2024) 2309819.

[5] D. Zhang, Y. Shi, H. Zhao, W. Qi, X. Chen, T. Zhan, S. Li, B. Yang, M. Sun, J. Lai, B. Huang, L. Wang, The facile oil-phase synthesis of a multi-site synergistic high-entropy alloy to promote the alkaline hydrogen evolution reaction, Journal of Materials Chemistry A, 9 (2021) 889-893.

[6] D. Wu, K. Kusada, T. Yamamoto, T. Toriyama, S. Matsumura, I. Gueye, O. Seo, J. Kim, S. Hiroi, O. Sakata, S. Kawaguchi, Y. Kubota, H. Kitagawa, On the electronic structure and hydrogen evolution reaction activity of platinum group metal-based high-entropy-alloy nanoparticles, Chemical Science, 11 (2020) 12731-12736.

[7] F. McKay, Y. Fang, O. Kizilkaya, P. Singh, D.D. Johnson, A. Roy, D.P. Young, P.T. Sprunger, J.C. Flake, W.A. Shelton, Y. Xu, CoCrFeNi High-Entropy Alloy as an Enhanced Hydrogen Evolution Catalyst in an Acidic Solution, The Journal of Physical Chemistry C, 125 (2021) 17008-17018.

[8] G. Feng, F. Ning, J. Song, H. Shang, K. Zhang, Z. Ding, P. Gao, W. Chu, D. Xia, Sub-2 nm Ultrasmall High-Entropy Alloy Nanoparticles for Extremely Superior Electrocatalytic Hydrogen Evolution, Journal of the American Chemical Society, 143 (2021) 17117-17127.

[9] P. Ma, M. Zhao, L. Zhang, H. Wang, J. Gu, Y. Sun, W. Ji, Z. Fu, Self- supported high-entropy alloy electrocatalyst for highly efficient H_2 evolution in acid condition, Journal of Materiomics, 6 (2020) 736-742.

[10] Z. Jia, K. Nomoto, Q. Wang, C. Kong, L. Sun, L.-C. Zhang, S.-X. Liang, J. Lu, J.J. Kruzic, A Self-Supported High-Entropy Metallic Glass with a Nanosponge Architecture for Efficient

Hydrogen Evolution under Alkaline and Acidic Conditions, Advanced Functional Materials, 31 (2021) 2101586.

[11] A. Asghari Alamdari, H. Jahangiri, M.B. Yagci, K. Igarashi, H. Matsumoto, A. Motallebzadeh, U. Unal, Exploring the Role of Mo and Mn in Improving the OER and HER Performance of CoCuFeNi-Based High-Entropy Alloys, ACS Applied Energy Materials, 7 (2024) 2423-2435.

[12] Z. Chen, J. Wen, C. Wang, X. Kang, Convex Cube-Shaped $Pt_34Fe_5Ni_{20}Cu_{31}Mo_9Ru$ High Entropy Alloy Catalysts toward High-Performance Multifunctional Electrocatalysis, Small, 18 (2022) 2204255.

[13] L. Li, H. Xuan, J. Wang, X. Liang, Y. Li, Z. Han, L. Cheng, Nanoporous nonprecious multi-metal alloys as multisite electrocatalysts for efficient overall water splitting, International Journal of Hydrogen Energy, 97 (2025) 38-45.

[14] S. Wang, H. Yan, W. Huo, A. Davydok, M. Zając, J. Stępień, H. Feng, Z. Xie, J.K. Shang, P.H.C. Camargo, J. Jiang, F. Fang, Engineering multiple nano-twinned high entropy alloy electrocatalysts toward efficient water electrolysis, Applied Catalysis B: Environment and Energy, 363 (2025) 124791.

[15] V. Buravets, E. Miliutina, V. Burtsev, K. Severa, V. Shilenko, J. Rosenkranzova, P. Hönicke, T. Hrbek, V. Svorcik, O. Lyutakov, High entropy 2D metals sulfides: Fast synthesis, exfoliation and electrochemical activity in overall water splitting at alkaline pH, Applied Surface Science, 681 (2025) 161600.

[16] B. Wen, X. Zhao, Q. Dong, B. Li, X. Lyu, Gradient composition design of FeCoCrMnNi high entropy alloys: An efficient and stable electrocatalyst for water splitting, Journal of Power Sources, 627 (2025) 235804.

[17] C.E. Park, J. Theerthagiri, V. Maheskumar, A. Kumar, G.H. Jeong, M.Y. Choi, Cocktail Effect of 4d/5d Band Twisted High-Entropy Alloys on Carbon Nanotube for Hydrazine Splitting, Small, n/a (2025) 2410304.

[18] Y. Jin, X. Fan, Q. Li, M. Guo, J. Bai, H. Lin, Y. Pi, S. Cao, C.-C. Hou, S. Bai, Self-Reconstruction of High Entropy Alloys for Efficient Alkaline Hydrogen Evolution, Small, n/a (2025) 2408165.

[19] X. Ma, Y. Zhou, S. Zhang, W. Lei, Y. Zhao, C. Shan, 3d–5d Orbital Hybridization in Nanoflower-Like High-Entropy Alloy for Highly Efficient Overall Water Splitting at High Current Density, Small, n/a (2025) 2411394.

[20] Y. Zhang, K. Nie, B. Li, L. Yi, C. Hu, Z. Wang, X. Hao, W. Zhang, Z. Liu, W. Huang, Cerium-optimized platinum-free high-entropy alloy nanoclusters for enhanced ampere-level sustainable hydrogen generation, Applied Catalysis B: Environment and Energy, 360 (2025) 124529.

[21] Z.-L. Wang, G.-Y. Huang, G.-R. Zhu, H.-C. Hu, C. Li, X.-H. Guan, H.-B. Zhu, La-exacerbated lattice distortion of high entropy alloys for enhanced electrocatalytic water splitting, Applied Catalysis B: Environment and Energy, 361 (2025) 124585.

[22] H. Xu, Y. Liu, K. Wang, L. Jin, J. Chen, H. Chen, G. He, High-entropy layered double hydroxides tailor Pt electron state for promoting acidic hydrogen evolution reaction, Journal of Colloid and Interface Science, 684 (2025) 566-574.

[23] H.-J. Qiu, G. Fang, J. Gao, Y. Wen, J. Lv, H. Li, G. Xie, X. Liu, S. Sun, Noble Metal-Free Nanoporous High-Entropy Alloys as Highly Efficient Electrocatalysts for Oxygen Evolution Reaction, ACS Materials Letters, 1 (2019) 526-533.

[24] A.L. Maulana, P.-C. Chen, Z. Shi, Y. Yang, C. Lizandara-Pueyo, F. Seeler, H.D. Abruña, D. Muller, K. Schierle-Arndt, P. Yang, Understanding the Structural Evolution of IrFeCoNiCu

High-Entropy Alloy Nanoparticles under the Acidic Oxygen Evolution Reaction, Nano Letters, 23 (2023) 6637-6644.

[25] S.-Y. Li, T.X. Nguyen, Y.-H. Su, C.-C. Lin, Y.-J. Huang, Y.-H. Shen, C.-P. Liu, J.-J. Ruan, K.-S. Chang, J.-M. Ting, Sputter-Deposited High Entropy Alloy Thin Film Electrocatalyst for Enhanced Oxygen Evolution Reaction Performance, Small, 18 (2022) 2106127.

[26] J. Tang, J.L. Xu, Z.G. Ye, X.B. Li, J.M. Luo, Microwave sintered porous CoCrFeNiMo high entropy alloy as an efficient electrocatalyst for alkaline oxygen evolution reaction, Journal of Materials Science & Technology, 79 (2021) 171-177.

[27] P. Yang, Y. Shi, T. Xia, Z. Jiang, X. Ren, L. Liang, Q. Shao, K. Zhu, Novel self-supporting thin film electrodes of FeCoNiCrMn high entropy alloy for excellent oxygen evolution reaction, Journal of Alloys and Compounds, 938 (2023) 168582.

[28] Z. Jin, J. Lv, H. Jia, W. Liu, H. Li, Z. Chen, X. Lin, G. Xie, X. Liu, S. Sun, H.-J. Qiu, Nanoporous Al-Ni-Co-Ir-Mo High-Entropy Alloy for Record-High Water Splitting Activity in Acidic Environments, Small, 15 (2019) 1904180.

[29] R. He, L. Yang, Y. Zhang, X. Wang, S. Lee, T. Zhang, L. Li, Z. Liang, J. Chen, J. Li, A. Ostovari Moghaddam, J. Llorca, M. Ibáñez, J. Arbiol, Y. Xu, A. Cabot, A CrMnFeCoNi high entropy alloy boosting oxygen evolution/reduction reactions and zinc-air battery performance, Energy Storage Materials, 58 (2023) 287-298.

[30] Y. Mei, Y. Feng, C. Zhang, Y. Zhang, Q. Qi, J. Hu, High-Entropy Alloy with Mo-Coordination as Efficient Electrocatalyst for Oxygen Evolution Reaction, ACS Catalysis, 12 (2022) 10808-10817.

[31] C. Zhao, W. Cai, N. Sun, S. Chen, W. Jing, C. Zhao, Facile preparation of porous high-entropy alloy FeCoNiCuMn and its OER performance, Journal of Physics and Chemistry of Solids, 184 (2024) 111668.

[32] X. Zhu, W. Huang, L. Tan, Z. Yao, X. Yang, R. Song, M. Chen, D. Liu, J. Zeng, H. Zhu, S. Lan, Ultrafast synthesis of tetragonal-distorted FeCoNiCuCr high-entropy alloy nanoparticles for enhanced OER performance, Chinese Chemical Letters, (2025) 110852.

[33] F. Miao, T. Wang, Z. Jing, Z. Zhang, J. Wang, T. Gu, Z. Yan, X. Liang, A dual-phase PtNiCuMnMo high-entropy alloy as high-performance electrocatalyst for oxygen evolution reaction, Applied Surface Science, 684 (2025) 161865.

[34] X. Hao, Y. Qi, S. Ding, S. Ma, B. Xu, B. Zhang, Q. Cao, P. Zhao, Facile synthesis of Ir-based high-entropy alloy nanomaterials for efficient oxygen evolution electrocatalysis, Journal of Colloid and Interface Science, 683 (2025) 1096-1105.